JOURNAL OF GEOPHYSICAL RESEARCH, VOL. 106, NO. B8, PAGES 16,549–16,566, AUGUST 10, 2001

Three-dimensional normal faulting models of the Valles Marineris, Mars, and geodynamic implications

Richard A. Schultz
Geomechanics-Rock Fracture Group, Department of Geological Sciences, Mackay School of Mines
University of Nevada, Reno, Nevada, USA

Jian Lin
Department of Geology and Geophysics, Woods Hole Oceanographic Institution, Woods Hole, Massachusetts, USA

Abstract. Inversion of Martian topography, using a three-dimensional boundary element model, permits revised estimates of fault dip angle, depth of faulting, paleogeothermal gradient, and extensional strain in the Valles Marineris region. The major normal faults dip at 40°–55° to depths of ~60–75 km with comparatively small footwall uplifts (< 500 m for throws to 10 km), implying that paleogeothermal gradients during faulting were ~10 K km^{-1} or less, assuming relatively rapid strain rates appropriate to the extending Martian crust. Accumulation of dip-slip offsets along the main normal faults likely was associated with anticlinal flexure and deformation of preexisting strata within the troughs. The magnitudes of the predicted vertical and horizontal displacements outside the troughs, as well as extensional strains, are spatially variable, depending on both cross- and along-strike position relative to the troughs. The predicted displacements and strains attain maximum values at the troughs and decay to background values at cross-strike distances of ~250 km, corresponding to 3–4 times the depth of faulting, with an average province-wide strain of 4–15%. By implication, the aggregate strain field surrounding Tharsis is a highly variable spatial and temporal composite of the inhomogeneous strain fields, each associated and scaling in size with an individual graben, from the smallest structures through the largest Valles Marineris troughs.

1. Introduction

The Valles Marineris system of normal-fault-bounded troughs contains the largest grabens on Mars [e.g., *Blasius et al.*, 1977; *Banerdt et al.*, 1992; *Schultz*, 1997]. These structures have developed relatively recently in Martian geologic history [*Witbeck et al.*, 1991; *Lucchitta et al.*, 1992; *Schultz*, 1998a], thus only modest amounts of erosion and deposition obscure their structural topography and morphology. Newly acquired precision topographic measurements made using the Mars Orbiter Laser Altimeter (MOLA) installed on the Mars Global Surveyor (MGS) spacecraft, combined with a three-dimensional (3-D) mechanical boundary element model of normal faulting, permit a geodetic inversion of the topography for these large structures. The results shed new light on the crustal structure beneath Valles Marineris and the geodynamic development of the Tharsis region.

In this paper, we explore the influence of normal faulting in the Valles Marineris by using a 3-D mechanical model that relates dip-slip fault offsets to deformation and stress changes in the surrounding Martian crust. We extract topographic characteristics of the trough system using newly acquired data from MOLA. These topographic constraints, along with the magnitudes of cumulative normal fault offset inferred along the major trough-bounding faults, permit an inversion of topography for the unique, best fitting parameters for particular faults, including dip angle and depth. The full set of fault parameters for the entire Valles Marineris trough system is then used to calculate predicted deformation and changes in cumulative Coulomb failure stress for the planetary surface. The resulting maps of fault-related uplift, horizontal extension, horizontal strain, and Coulomb stress change are discussed in light of the geodynamic evolution of the Tharsis region.

Paper number 2001JB000378.
0148–0227/01/2001JB000378$09.00

2. Background on Valles Marineris

The Valles Marineris system of trough depressions is a complex, polyphase suite of partially filled structural basins (see *Lucchitta et al.* [1992] and *Schultz* [1998a, 2000a] for review). The latest phase of deformation, discussed and investigated in this paper, is represented by a series of large grabens that, while perhaps best described as lithospheric rift basins [e.g., *Banerdt et al.*, 1992; *Anderson and Grimm*, 1998; *Schultz*, 2000a], are remarkably devoid of volcanism and basin-filling deposits that could otherwise obscure their structural and topographic signatures [e.g., *Witbeck et al.*, 1991; *Lucchitta et al.*, 1994]. These troughs (or grabens) attain aggregate lengths of several hundred kilometers and widths of several tens of kilometers [*Blasius et al.*, 1977], with depths approaching 10 km [*Smith et al.*, 1999]. The main troughs are associated with numerous smaller grabens on adjacent plateaus (Figure 1) having a variety of spacings, lengths, and orientations [*Schultz*, 1997, 2000a] that may locally predate the main trough depressions [*Witbeck et al.*, 1991]. The troughs are oriented subradial to the center of Tharsis, as are other radial graben sets elsewhere on the Martian western hemisphere [e.g., *Carr*, 1974; *Plescia and Saunders*, 1982], implying a roughly circumferential extensional strain field about the Tharsis region [*Banerdt et al.*, 1992] during their development.

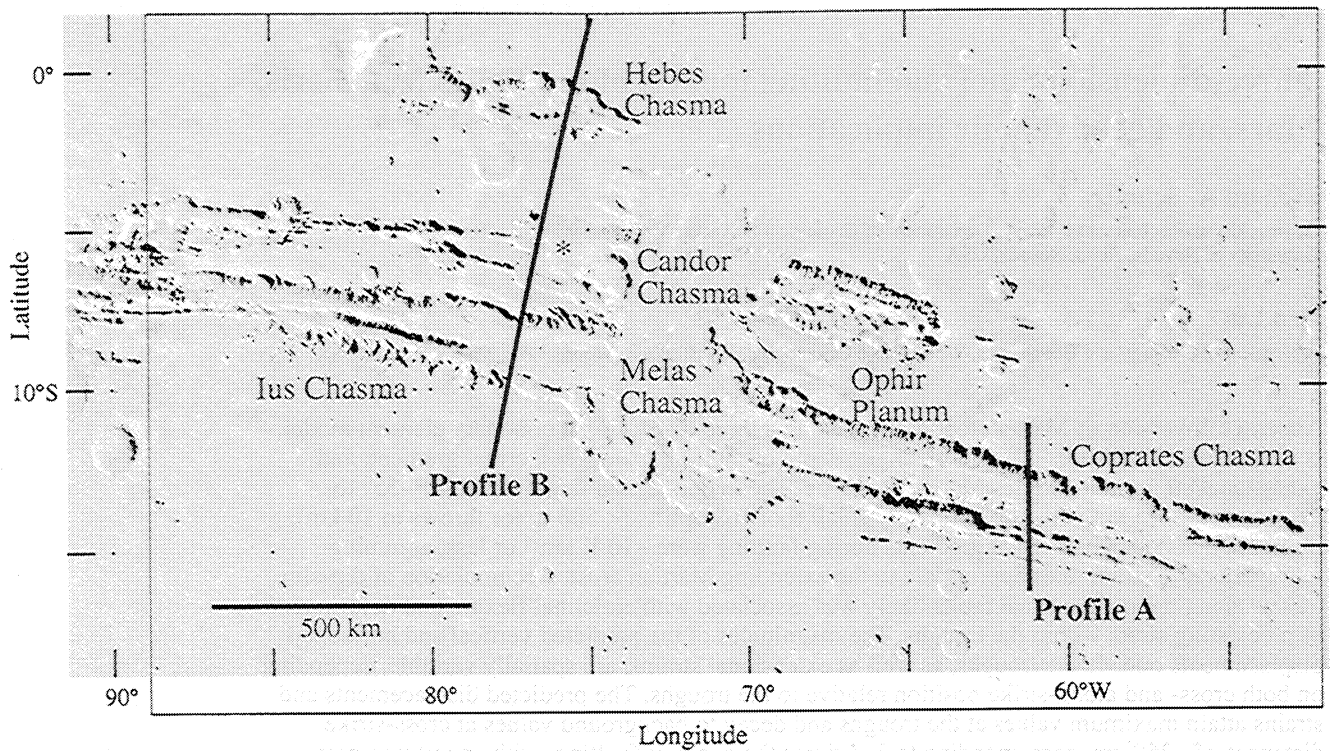

Figure 1. Location map showing major named troughs and profiles A and B in the Valles Marineris region. Box shows calculation grid (Figures 7, 8, and 9). Asterisk indicates location of Candor Mensa.

The Valles Marineris Extensional Province is developed along the eastern part of the larger Tharsis volcanotectonic assemblage. Tharsis is a long-lived locus of successive phases of volcanism and tectonism that affect nearly one half of the surface area of Mars [e.g., *Carr*, 1974; *Plescia and Saunders*, 1982; *Tanaka et al.*, 1991; *Banerdt et al.*, 1992; *Mège and Masson*, 1996a]. In general, older concentric arrays of contractional structures ("wrinkle ridges" [*Watters*, 1993; *Schultz*, 2000b]) are overprinted by younger, radially oriented sets of narrow grabens [*Tanaka et al.*, 1991]. Several smaller areas associated with their own radial and concentric normal faults and grabens, such as Syria Planum, are nested within the larger Tharsis province, contributing to a complex superposition of structures and stress states. *Tanaka et al.* [1991], *Mège and Masson* [1996a], and *Smith et al.* [1999] discuss possible geodynamic scenarios for the development of the Tharsis.

The overall geologic development of the Valles Marineris region is well understood [e.g., *Witbeck et al.*, 1991]. Volcanotectonic activity, centered initially to the west in Syria Planum [*Frey*, 1979; *Plescia and Saunders*, 1982; *Tanaka and Davis*, 1988; *Mège and Masson*, 1996b] and to the south in Thaumasia [*Dohm and Tanaka*, 1999], was active from perhaps late Noachian through early Hesperian time. This early phase of activity is associated with attainment of high regional topography and crustal thickening [*Anderson and Grimm*, 1998; *Dohm et al.*, 1998] (perhaps visible as discrete layers as recently identified in Mars Orbiter Camera (MOC) images by *McEwen et al.* [1999]), fissure-fed lava plains extrusion [*Mouginis-Mark et al.*, 1992], subsurface dike emplacement [*Mège and Masson*, 1996b], growth of the early Hesperian sets of radial grabens [*Tanaka et al.*, 1991], and wrinkle ridge deformation [e.g., *Watters*, 1993; *Schultz*, 2000b]. During the succeeding phase a widespread hydrologic system was apparently active in the Valles Marineris region. Subsurface and surface fluid flow is associated with a variety of large-scale landforms during late Hesperian time, including ancestral basins (closed trough depressions [*Spencer and Fanale*, 1990]), accumulation of interior layered deposits ("basin beds") [*Lucchitta et al.*, 1992, 1994], and formation of chaotic terrain and catastrophic outflow channels [e.g. *Baker et al.*, 1992; *Komatsu et al.*, 1993]. Progressive desiccation and/or freezing of subsurface aquifers [*Clifford*, 1993; *Carr*, 1999] may have occurred into early Amazonian time.

In the latest stage, during latest Hesperian or Amazonian time [*Schultz*, 1998a], regionally distributed stresses associated with classical Tharsis-centered deformation [e.g., *Banerdt et al.*, 1992] induced crustal extension visible at the surface surrounding Tharsis, producing a second set of Tharsis radial grabens [e.g., *Carr*, 1974; *Plescia and Saunders*, 1982; *Tanaka et al.*, 1991] and larger structures such as Valles Marineris (the "rectangular" structural troughs [*Schultz*, 1991, 2000a; *Lucchitta et al.*, 1992]) and the Thaumasia graben [*Plescia and Saunders*, 1982; *Tanaka and Davis*, 1988]. Landslides [*Lucchitta*, 1979; *McEwen*, 1989; *Dade and Huppert*, 1998] suggest geologically recent slope failures along the major trough-bounding normal faults in the central Ius-Melas-Coprates graben [*Schultz*, 1995a, 1998a, 1998b; *Mège and Masson*, 1996c]. The slope failures represent some of the most recent activity within the troughs, approximately coeval with emplacement of young interior deposits over previously tilted basin beds [*Lucchitta*, 1990]. A mechanical analysis of the influence of the major trough-bounding normal faults on deformation and stress changes of the Martian surface is the central purpose of this paper.

3. Modeling Approach

In order to investigate the relationship between normal faulting at Valles Marineris and deformation of the surface we adopt standard techniques of geodetic inversion of fault-related topography [e.g.,

Cohen, 1999]. Given independent estimates of surface topography, forward mechanical models are used to calculate the displacements of surface rocks due to prescribed fault geometries and offset magnitudes. A good correspondence between the calculated and observed topographies would suggest that the fault parameters obtained in the model adequately represent the Martian fault characteristics. Deformation of the planetary surface surrounding a normal fault array produces a spatially varying, inhomogeneous displacement field [e.g., *Ma and Kuznir*, 1993; *Taboada et al.*, 1993], and we demonstrate that the calculated quantities vary in magnitude, and spatially, relative to the troughs.

3.1. MOLA Topography Across Valles Marineris

The topography of the Valles Marineris trough region has been substantially revised through the acquisition of precision data from the Mars Global Surveyor spacecraft and the Mars Orbiter Laser Altimeter (MOLA) [*Zuber et al.*, 1992; *Smith et al.*, 1999; *Ladbury*, 1999]. Prior to MOLA, elevations were determined (with considerably larger uncertainties) by using combinations of stereophotogrammetry, stellar occultation data, and Earth-based radar.

We calculated values for the cross-sectional topographic relief across the troughs by using the MOLA data available to the scientific community during late 1999. These data include one MOLA profile (part of orbit 25 available from the MGS Science Sampler CD: http://mars.jpl.nasa.gov/mgs/sci/Cdsampler/browse/mola.htm [*Smith et al.*, 1998]) that crosses the west central part of the trough system between 77° and 76°W and ~3°–11°S (profile B, Figure 1) and the 1°x1° digital elevation model (DEM) of the region's topography [*Smith et al.*, 1999; *Ladbury*, 1999] produced by the MOLA team from data interpolated between successive orbital tracks (grid spacing ~59 km). Values of topographic relief for each trough were obtained by subtracting the elevations of the trough floor [*Smith et al.*, 1999] in the main, composite Ius-Melas-Coprates Chasma [*Lucchitta et al.*, 1994; *Mège*, 1994; *Mége and Masson*, 1996c; *Schultz*, 1995a, 1997, 1998a] from those of the adjacent plateaus (Figure 2a). In this central, composite graben, trough floors appear to be only thinly mantled by surficial deposits [e.g., *Lucchitta et al.*, 1994; *Schultz*, 1998b], in contrast to other, nearby troughs such as southern Melas Chasma, Ophir and Candor Chasmata, and Hebes Chasma that all contain variable or substantial thicknesses (> 3 km) of layered deposits [*Nedell et al.*, 1987; *Witbeck et al.*, 1991; *Lucchitta et al.*, 1992, 1994]. Trough floors (in the Ius-Melas-Coprates Chasma composite graben) are observed to be correlative (or nearly so) with ridged plains materials that cap the adjacent plateaus [*Lucchitta et al.*, 1994; *Schultz*, 1991, 1997, 1998b]. Thus the topographic relief, measured as the difference in elevation between the plateau and floor, defines the vertical component of cumulative structural offset ("throw") across the major trough-bounding normal faults in Valles Marineris. This set of known throws is a primary constraint in the boundary element modeling.

A MOLA-based map of trough relief, shown in Figure 2b, reveals variations in the throws associated with the northern and southern (fault) walls of the composite Ius-Melas-Coprates Chasma trough. The trough elevations and relief from the DEM agree well with the precise measurements extracted from the single MOLA profile (Figure 1, profile B; see Figure 6). We find that the fault throws vary systematically with along-strike position, in agreement with previous determinations that used Viking-based topography [*Mège*, 1994; *Schultz*, 1995a, 1997; *Mège and Masson*, 1996c] (Figure 2b). The dip-slip throw for both the northern and southern trough walls is greatest at ~65°W, in Coprates Chasma, and is minimum at the

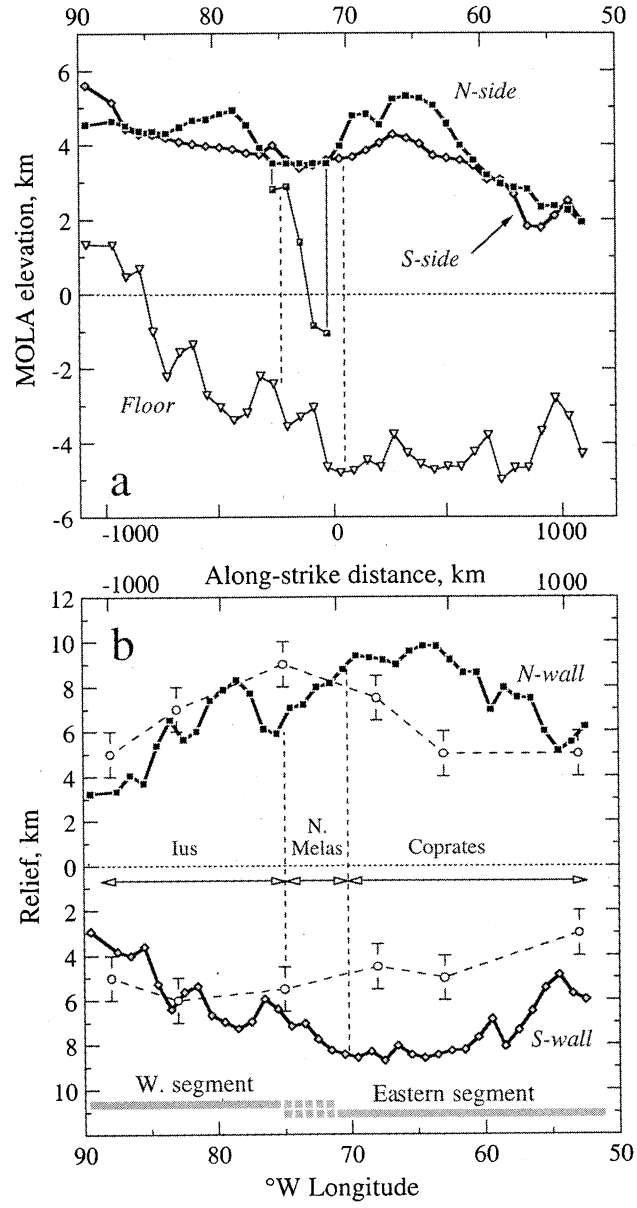

Figure 2. (a) MOLA elevations of trough floor (open triangles) and bounding northern (solid squares) and southern plateaus (open diamonds) of composite Ius-Melas-Coprates Chasmata graben. Half-solid squares show details of trough structure not adequately resolved by the 1°x1° MOLA gridded data set. (b) Stratigraphic cutoff diagrams showing inferred structural throws (solid curves) between plateau caprock and trough floor. Viking-based estimates of along-strike structural relief are open symbols with dashed curves; data are from *Schultz* [1995a]. Note the dual maxima, at 80° and 65°W, apparent on both sides of the composite trough. Top part of Figure 2b is northern plateau; lower part is southern plateau. Note that the vertical scale for relief along the southern wall has been inverted in Figure 2b for clearer comparison with that along the northern wall.

trough ends. However, the new MOLA elevations demonstrate a more systematic and smoothly varying distribution along the length of the trough system than was previously revealed using Viking data (see Figure 2b). For example, the along-strike throw increases from minimum values of 5–6 km near the trough ends [e.g., *Smith*

et al., 1999] to a maximum value of 9–10 km (Figure 2b) near its center. However, the MOLA data reveal a secondary maximum of ~8 km located in central Ius Chasma (Figures 2a and 2b) that is more pronounced for the northern wall than for the southern wall.

The gridded MOLA data used for this analysis appear too coarse to adequately resolve certain elements of trough physiography. For example, the east sloping plateau segment that separates Candor Chasma to the north from central Melas Chasma to the south is only 1°–2° (~60–120 km) wide. The gridded MOLA data do not resolve this structure as well as the later 1/16th degree data (qualitatively presented by *Ladbury* [1999]), leading to uncertainties in its topography. Because this sloping plateau segment partially defines the northern wall of the composite structural trough, these uncertainties (half-solid squares in Figure 2a) contribute to some imprecision in both the along-strike variation in plateau elevations (Figure 2a) and the associated trough relief (Figure 2b). More importantly, however, this plateau segment may have been deformed by a subsequent phase of deformation that breached the two troughs [e.g., *Lucchitta et al.*, 1994]. We choose to estimate the original plateau segment elevations by extrapolating the topography horizontally across the northern Melas Chasma area onto Ophir Planum (solid squares in Figure 2a).

In general, throws along the northern and southern walls appear comparable in magnitude and distribution, with the maximum throws larger along the northern walls (Figure 2b, upper panel) than along the southern walls (Figure 2b, lower panel with inverted scale to show symmetry with northern wall's throw distribution). Previous estimates based on Viking data [*Schultz*, 1995a; *Mége and Masson*, 1996c] placed the maximum trough depth in westernmost Coprates Chasma or central Melas Chasma, near the composite trough's midpoint, with considerably smaller values of trough relief inferred along the southern walls (Figure 2b). The MOLA-based data, however, demonstrate that the maximum value of throw is located ~450 km east of the trough midpoint, with a secondary maximum located ~500 km to the west of the midpoint. These dual maxima, in conjunction with the form of the along-strike throw distribution, suggest that the composite trough may represent two linked segments (Figure 2b, lower panel, shaded bars), each with its own respective maximum [*Schultz*, 2000a], rather than one single graben.

3.2. Boundary Element Model

We use the three-dimensional mechanical boundary element model Coulomb (available at http://quake.usgs.gov/research/deformation/modeling/coulomb; see *King et al.* [1994] and *Toda et al.* [1998] for applications of this computational approach to tectonic problems), which uses the stress functions derived by *Okada* [1992], to relate deformation of the planetary surface to the cumulative, geologic offsets along the major Valles Marineris faults. In our calculations the magnitude of cumulative dip-slip offset D is prescribed along a particular fault in the system (using Figure 2b and the individual fault traces, e.g., *Schultz* [2000a]), which has a specified geometry (map view length L, dip angle δ, downdip height

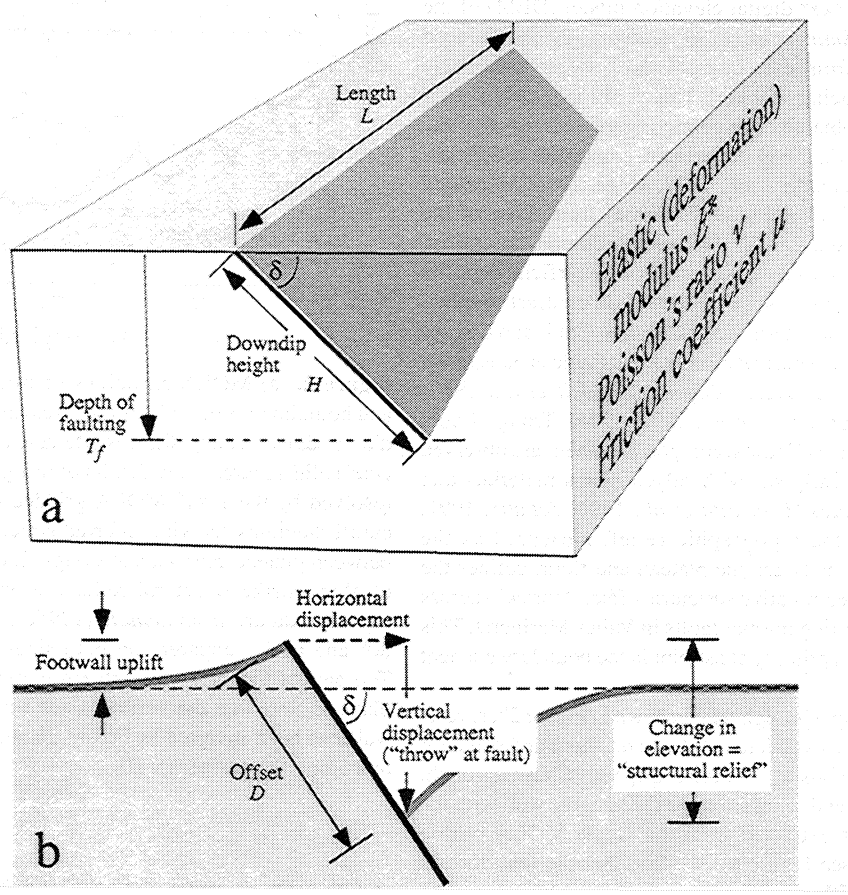

Figure 3. Definition of terms used in this study. (a) Fault geometry parameters L, H, T_f, and δ with half-space parameters E^*, ν, and μ. (b) Relationship between cumulative fault offset D, dip angle δ, throw, relief, and structural uplift of the footwall for a single normal fault.

Table 2. Best Fitting Parameters for Valles Marineris Faults

Trough[a]	Fault[b]	Profile	Depth T_f, km	Fault Dip δ, deg	Offset D, km	Downdip Height[c] H, km	Moment[d], M_G, 10^{24} N m
Candor							
N wall, W	1	B	75	45°S	6	106	1.1
N wall, E	2	D	75	45°S	6	106	1.3
Ant. W[e]	3	B	60	55°N	2	73	0.23
Ant. E	4	D	60	55°N	2	73	0.26
S wall, W	5	B	75	45°N	6	106	0.98
S wall, E	6	D	75	45°N	6	106	1.1
Ius							
N wall, W	7	G	60	45°S	6	85	0.65
N wall, center	8	F	75	45°S	6	106	0.89
N wall, E	9	B	75	45°S	8	106	1.3
S wall, W	15	G, F	60	40°N	6	93	1.2
S wall, E	16	B	75	40°N	6	117	0.87
Melas							
N wall, W	10	–	75	55°SW	8	92	0.10
N wall, E	11	D	75	45°SW	8	106	0.76
S scarp	17	E, D	75	40°N	6	117	1.2
Coprates							
N wall, W	12	C	75	55°S	12	92	1.2
N wall, center	13	A	75	55°S	10	92	1.3
N wall, E	14	H	75	55°S	6	92	0.79
S wall	18	C, A	75	40°N	12	117	5.9

[a] N wall, northern wall; S wall, southern wall; Ant., antithetic fault; S scarp, southern scarp.

[b] Fault numbers keyed to Figure 7.

[c] Downdip fault height H = (depth of faulting)/[sin (fault dip angle)]; see Figure 3a.

[d] Total geologic moment $M_G \equiv GAD$, where G = 4 GPa (shear modulus), A is fault area (map length L x downdip height H), and D is average cumulative geologic offset.

[e] North facing antithetic fault within subsidiary graben in northern Candor Chasma.

H) and position (in map view, relative to the trough system) in an elastic half-space (Figure 3a); the offset D along the fault induces displacements and stress changes in the material surrounding it [e.g., *Bruhn and Schultz*, 1996; *Cohen*, 1999]. The final fields of predicted displacement and Coulomb stress change for the Martian surface are the sum of the individual fields from each model fault.

Precision measurements of the structural trough relief from MOLA provide tight bounds on the magnitudes and along-strike distribution of normal fault throws that are used in the model. By prescribing the fault throws, the other free parameters (fault dip δ and fault depth T_f) can vary within only a narrow range, leading to a unique solution for the fault's geometric properties in cross section (for given values of modulus and Poisson's ratio). As discussed in section 3.3.5, the absence of significant trough flank uplifts argues against both very steep ($\delta > 55°$) and very shallow (less deep; $\delta < 60$ km) faults (having the magnitudes of throws given by the MOLA data, Figure 2b). The resulting distribution of displacements and cumulative Coulomb stress change for the planetary surface, calculated once the faults' geometric parameters have been obtained from the full 3-D solution, are generally consistent with those that would be obtained from a full mechanical solution for the fault parameters (offset D, dip angle δ, and downdip height H, or vertical depth T_f) that additionally must specify the 3-D stress state in the Martian lithosphere and the constitutive relations (e.g., friction, pore pressure distribution, surface roughness, rate and state variables) of the faults [e.g., *Rudnicki*, 1980; *Cohen*, 1999]. Because the magnitude and depth distribution of stress associated with trough development are unknown for Mars, we choose to model fault-related topography and surface deformation by using a dislocation model that uses the observed fault configuration (map length, throw, estimated dips; Figure 3b) as constraints. Although the dislocation approach we employ in this paper adequately represents the deformation and Coulomb stress changes in the Martian crust due to the cumulative dip-slip offsets along Valles Marineris normal faults, it neglects the influence on topography and stress change due to nonfault effects, such as crustal stress states and inelastic rheologies. The contribution of these far-field effects on deformation, strain, and Coulomb stress change near the surface should be small, however, compared to the effects of fault offsets, as suggested by previous work on terrestrial fault systems [e.g., *Freed and Lin*, 1998].

Elastic properties for the faulted half-space, appropriate for the near-surface region, are given by deformation modulus E^* = 10 GPa (equivalent to the Young's modulus parameter for crustal scales [*Schultz*, 1996]) and Poisson's ratio ν = 0.25. These values are comparable to those used to model deformation associated with

fault offset in the terrestrial continental crust [e.g., *Freed and Lin*, 1998] (Table 1). We use a constant value of dip-slip offset D along each fault segment, with each segment idealized as a rectangular plane having horizontal length L, downdip height H, dip angle δ, and vertical depth of faulting T_f (Figure 3a).

An elastic half-space solution was used to model the changes in surface displacement and cumulative Coulomb failure stress due to prescribed dip-slip offset along model faults. For Mars, no time-dependent data for fault offset rates (either incremental, for individual slip events, or cumulative, for total geologically observed offsets) or postseismic deformation are available. Terrestrial studies suggest that longer-term deformation due to fault afterslip or viscous relaxation of subjacent lower crust or mantle rocks contributes to displacements at the surface that are perhaps 1–2 orders of magnitude smaller than the coseismic values [*Freed and Lin*, 1998; *Cohen*, 1999]. Layered systems involving an elastic plate over an inviscid or homogeneously deforming substrate may be unrealistic representations of crustal behavior in the vicinity of trough faults. Stress gradients that are generated locally in the substrate because of fault offsets can profoundly increase or decrease the local rates of flow near the faults [*Freed and Lin*, 1998], leading to incomplete transfer of stress (from the entire substrate) to the overlying elastic crust, preferential softening around faults, and inhomogeneous strain rates. These effects render crustal strength envelopes (that assume homogeneous stresses and constant strain rates) unreliable in the proximity of faults [*Kirby and Kronenberg*, 1987; *Albert et al.*, 2000]. As discussed in section 3.3.5, the absence of significant trough flank uplifts at Valles Marineris argues against large reductions in viscosity (or presence of ductile layers) in the crust below the troughs. As a result, an elastic analysis is considered as a good first-order approximation to capture the main characteristics of cumulative fault offset in the Martian crust.

3.3. Sensitivity of Topography to Fault Parameters

A series of 2-D calculations were performed to investigate the influence of key parameters on the topography associated with normal faulting in the troughs. Profile A (see Figure 1) was chosen as a reference for these calculations because (1) it cuts across the central part of Coprates Chasma where it is defined by only two major normal faults, and (2) the trough is long enough (L > 800 km) that variations in the along-strike (L, third) dimension may not be critically important. Vertical displacements calculated from the model (along a vertical slice perpendicular to, and through the approximate center of, the Coprates Chasma graben) are used to infer the topographic changes (uplift and subsidence) related to the cumulative dip-slip fault offsets. We first conducted a series of 2-D modeling runs to determine the sensitivity of predicted topography to key parameters including cumulative fault offset D, depth of faulting T_f, fault dip angle δ (Figure 3b), and the elastic properties of the faulted half-space (E^* and ν). On the basis of the results of these sensitivity studies, values for cumulative fault offset D, dip δ, and depth T_f were then adjusted for each fault within the total 3-D Valles Marineris model until the best fit to the observed topography was achieved.

Our reference case for the sensitivity study is a graben with two inwardly dipping normal faults. The graben is 60 km wide, with a master fault (labeled curves shown in Figures 4a, 4b, and 4c) and an antithetic fault (labeled curves shown in Figures 4a, 4b, and 4c) having a cumulative offset D consistently 1 km less than that on the master. This slightly asymmetric graben is based on the cross-sectional form of central Coprates Chasma. The provisional 1 km difference in cumulative fault offset is associated (by fault dip angle δ) with the difference in elevation across Coprates Chasma, along profile A (greater relief across the northern wall than across the southern wall; cf. Figure 2b). The vertical slice is coincident with the location of profile A (Figure 1).

3.3.1. Fault offset *D*. Increasing the magnitude of cumulative normal (dip-slip) offset D along the paired graben faults, while holding the other parameters constant, increases both the amplitude of uplifts that flank the troughs (Figure 3b; Figure 4a, right) and the depth of the trough floor (Figure 4a, left). Because the heights of flanking uplifts increase with fault offset, the structural relief (difference between maximum and minimum values across the fault; see Figure 3b) also increases. For example, increasing the offset from D = 10 to D = 12 km (along the master fault; offsets along the antithetic fault are 1 km less), while holding depth (T_f = 60 km) and fault dip (δ = 60°) constant, increases the height of uplift flanking the master fault from 1870 m to 2200 m, or 18% (Figure 4a, right), while graben floor depth increases from 6.8 to 8.2 km, a 21% increase (Figure 4a, left). Fault offset D influences the amplitude of displacement, but not the shape of the displacement profile, across the graben, for constant values of fault dip δ and depth T_f.

3.3.2. Fault dip δ. Variations in fault dip angle δ affect both the amplitude and shape of fault-related surface topography (Figure 4b). For constant depth (T_f = 60 km) and cumulative offset magnitude (D = 10 km along the master fault, D = 9 km along the antithetic fault), steeper dips promote flanking uplifts and upwardly bowed, dome-like graben floors, whereas shallower dips promote subhorizontal to trough-dipping flanks and convex downward, basin-like floors. These results are comparable to those reported previously by *King et al.* [1988]. For depth T_f = 60 km and offset D = 10 km (along the master fault), fault dips steeper than δ ~ 55° lead to flank uplifts (Figure 3b) and bowed graben floors (Figure 4b, right).

3.3.3. Depth of faulting T_f. The vertical depth of faulting T_f (Figure 3a) also influences both the amplitude and shape of the predicted topography. Shallower faults (smaller T_f, for constant dip δ and cumulative offset D) promote sharp flanking uplifts and upwardly bowed floors, whereas deeper faults (with the same values of dip and offset) inhibit flank uplift and promote flatter graben floors (Figure 4c). For constant values of cumulative offset magnitude (D = 10 km) and fault dip angle (δ = 60°), faults with depths T_f less than ~70 km (and associated downdip heights H of 81 km) produce significant flank uplifts (> 2 km in height) and bowed graben floors.

3.3.4. Elastic (deformation) modulus E^* and Poisson's ratio ν. Variations in the elastic modulus E^* for the faulted elastic half-space, from 1 to 100 GPa in the models, contribute to an insignificant change (< 10 m at maximum amplitude) in the calculated topography. Increasing Poisson's ratio ν from 0.2 to 0.5 leads to a small reduction in trough depth from 6.81 to 6.58 km (< 4%, assuming a D = 10 km offset, δ = 60° dip, and depth T_f = 60 km) and a somewhat larger increase in flank uplift in this case from 1.83 to 2.06 km (13%). Neither property is expected to change significantly with position along the trough system, so that constant values used in the calculations are expected to contribute an uncertainty of perhaps ±10% or less to the calculated topography across the troughs.

3.3.5. Parameter trade-offs. The most important parameters affecting the magnitude and shape of the predicted topography (once the magnitude of cumulative fault offset D is chosen) are fault dip δ and fault depth T_f. Both of these promote similar changes in the displacement profiles and both can trade off, leading to a unique

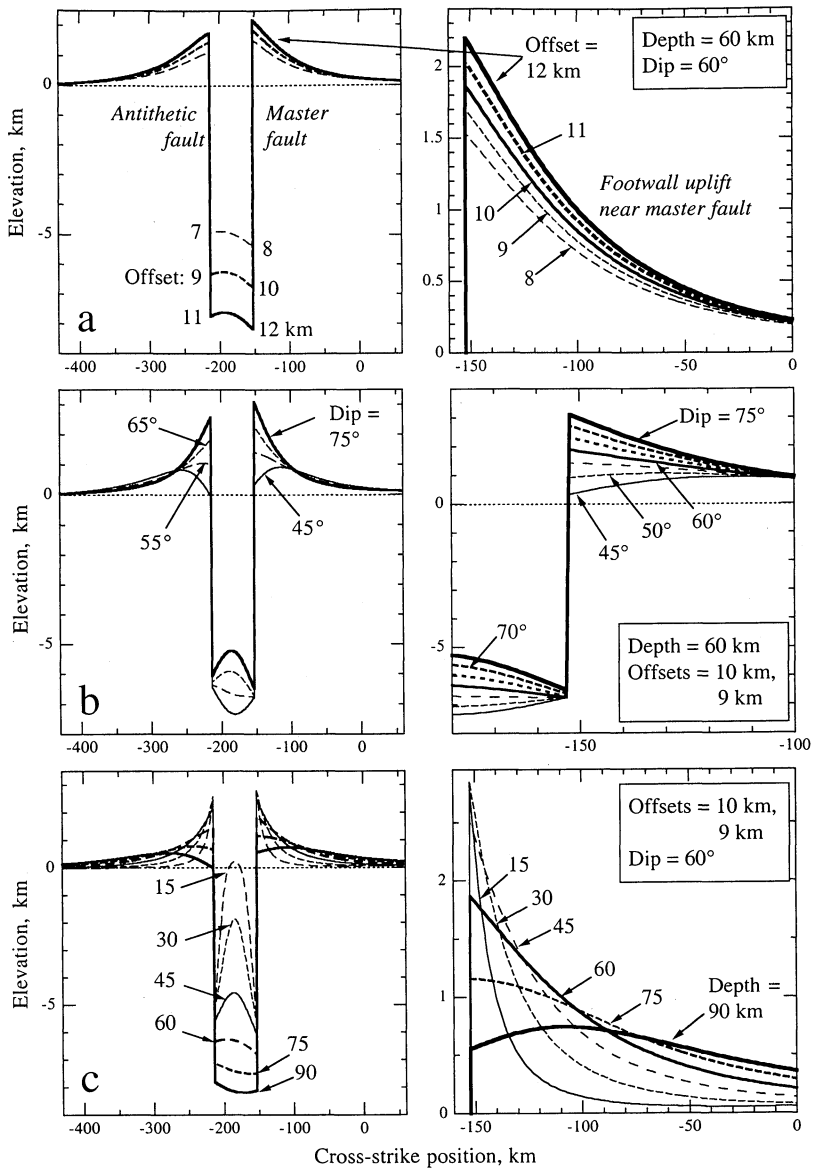

Figure 4. Trade-offs of key parameters from boundary element modeling of vertical displacements of the planetary surface for the two-fault graben, based on the geometry of central Coprates Chasma. (left) Full displacement profiles and (right) detail near master fault (northern) side of graben. (a) Effect of cumulative offset magnitude D along both faults on surface displacement (dip angle δ and depth T_f held constant). Master fault (numbers to right of curves) has 1 km consistently greater cumulative offset than the antithetic fault (numbers to left of curves). Master and antithetic faults both dip at $\delta = 60°$ and reach $T_f = 60$ km vertical depth. (b) Effect of dip angle δ (offset D and depth T_f constant). Master fault has $D = 10$ km cumulative offset and antithetic has $D = 9$ km; both reach $T_f = 60$ km depth. (c) Effect of fault depth T_f (dip angle δ and cumulative offset D constant). Master fault has $D = 10$ km cumulative offset and antithetic has $D = 9$ km; both dip at $\delta = 60°$.

range of permissible solutions to the observed topography. This trade-off is illustrated in Figure 5 by setting the cumulative fault offset (using a single normal fault) to $D = 10$ km, varying (in turn) the fault dip angle δ and depth T_f, calculating the predicted maximum vertical displacement of the footwall (see Figure 3b, assuming elastic parameters listed in Table 1), and contouring the values. The shaded region in Figure 5 (within labeled contours of predicted footwall topography) brackets the approximate range of values permitted by MOLA for footwall uplift flanking the larger Valles Marineris troughs [e.g., *Anderson and Banerdt*, 2000]; the two points (solid symbols) in Figure 5 represent particular values of footwall topography extracted along profile A (Figure 6a). Figure 5 shows that footwall uplifts of 0.5 to 1 km are consistent with normal faults having a $D = 10$ km dip-slip offset, dip angles δ between 55° and 60°, and vertical depths (T_f) between 60 and 75 km (using the elastic parameters listed in Table 1). As demonstrated in Figure 4, variations in the magnitude of cumulative dip-slip fault offset D modulate the amplitude of the topography associated with each paired combination of dip and depth. Variations in elastic properties of the faulted half-space contribute only a relatively small systematic uncertainty to the calculated topography.

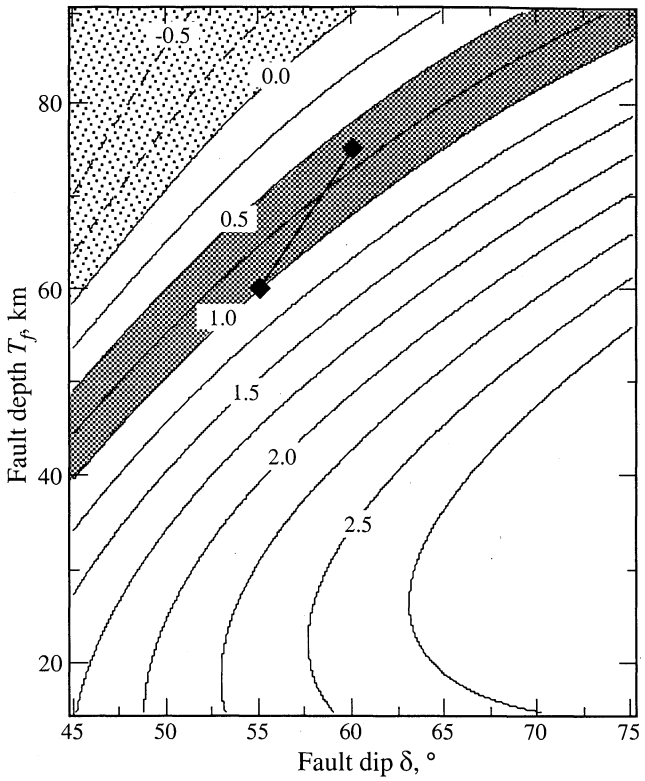

Figure 5. Contours of the predicted magnitude of footwall uplift as a function of variations in fault dip angle δ and fault depth T_f. A cumulative offset magnitude of D = 10 km along a single normal fault is assumed. Shaded band between 0.5 and 1.0 km shows maximum uplift permitted by MOLA topographic data for comparable troughs; stippled region shows area of potential footwall subsidence. Solid symbols represent MOLA data for footwall uplift (Figure 3b) observed across central Coprates Chasma (profile A).

4. Results

4.1. Comparison with Topographic Profiles A and B

The best fits to the topography along profile A (using the model configuration of section 3.3) are shown in Figure 6a. The data for profile A were extracted from the 1°x1° gridded data set. Acceptable fits to the MOLA data across central Coprates Chasma are obtained from the preliminary 2-D solution alone for fault depths T_f between 60 and 75 km and fault dips δ between 55° and 60°. These values assume a constant D = 10 km cumulative offset along the northern fault and a D = 9 km cumulative offset along the entire southern fault, with both faults using the same values of dip and depth during the model runs. Shallower depths of faulting (e.g., T_f < 45 km) and/or steeper fault dips lead to large flanking uplifts, with amplitudes exceeding 3 km within 100 km of the trough edge. Because such prominent flanking uplifts are not observed in this region or elsewhere along the troughs [*Schultz*, 1991; *Anderson and Grimm*, 1998; *Anderson and Banerdt*, 2000], substantially smaller depths of faulting, and steeper fault dips, do not appear to be consistent with the observed trough topography.

Comparison between the modeling results and the MOLA topography along profile A reveals that graben width can also provide an additional constraint on the fault parameters. For example, cumulative offset D along a shallowly dipping normal fault promotes upward displacement of near-surface rocks located vertically above the lower fault tip [e.g., *Bruhn and Schultz*, 1996], leading to locally increased surface elevations and anticlinal flexure there (Figure 4b). As a result, faults having shallow dips (δ) and/or depths (T_f) can promote higher topography and steeper slopes (away from the trough) of the opposing trough-bounding plateau, leading to poorer fits to the observed topography, because the lower fault tips are located directly beneath the opposing plateau. As a result, the measured trough widths supplement the MOLA topography in bounding the admissible range of fault parameters, leading in many cases to modifications in the parameters for the faults (e.g., in central Coprates Chasma).

A reanalysis of the topography along profile A using the complete set of faults in Coprates Chasma and the full, 3-D model modified the preliminary estimate of the fault parameters shown in Figure

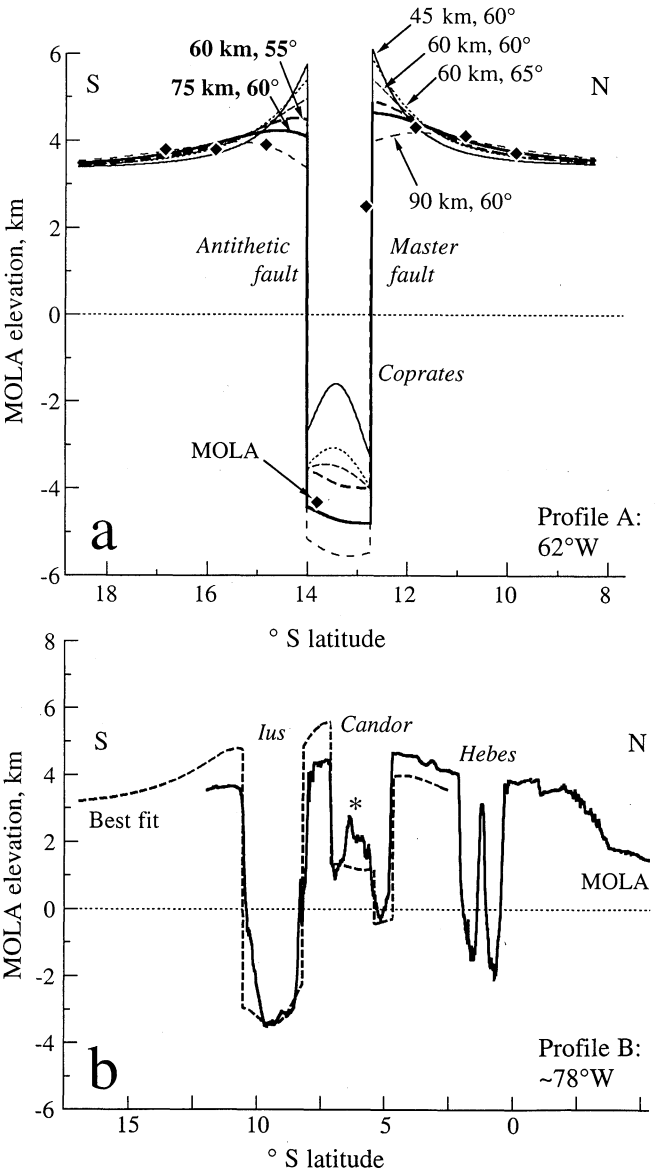

Figure 6. (a) Variation in fault parameters compared to MOLA topographic profile across eastern Valles Marineris troughs along profile A, central Coprates Chasma. Model is set up as in Figure 4. (b) Best fitting solution for fault parameters along profile B, central Ius and westernmost Candor Chasmata; MOLA data from orbit 25 [*Smith et al.*, 1998]. Asterisk indicates position of Candor Mensa.

Table 1. Parameters for Boundary Element Model

Parameter	Symbol	Values Investigated	Final Model Value(s)
Fault offset	D	1–15 km	2–12 km
Fault dip	δ	40°–75°	40°–55°
Fault depth	T_f	15–90 km	60–75 km
Deformation modulus	E^*	1–100 GPa	10 GPa
Poisson's ratio	ν	0.2–0.5	0.25
Friction coefficient	μ	0.2–0.8	0.4

6a and discussed in this section. A better match with the gridded MOLA topography on either side of Coprates Chasma was obtained by explicitly varying the magnitudes of cumulative fault offsets D along-strike, along both northern and southern sides, simulating (using trigonometric corrections for fault dip) the observed variations in trough relief (shown in Figure 2b). Combined with the trough width constraint just discussed, the best fitting parameters for the central part of Coprates Chasma (along profile A) are, for the northern wall (fault 13 on Table 2): cumulative dip-slip offset D = 12 km, dip angle δ = 55°S, and depth of faulting T_f = 75 km; for the opposing, southern wall (fault 18 on Table 2) the best fitting parameters are cumulative dip-slip offset D = 12 km, dip angle δ = 40°N, and depth of faulting T_f = 75 km.

Profile B crosses a more complex trough configuration along ~78°W, including the central part of Ius Chasma to the south and the westernmost part of Candor Chasma to the north (Figure 1). The MOLA track from orbit 25 [*Smith et al.*, 1998] reveals the topography much more precisely than do the interpolated 1° intervals available along profile A and elsewhere along the trough system. The MOLA topography suggests that the plateaus adjacent to Ius and western Candor Chasmata slope gently away from the troughs, but with no evidence for significant flanking uplifts. Trough floor in Ius Chasma appears either concave downward or gently sloping to the south. Interior layered deposits in Candor Chasma ("Candor Mensa"; near 7.5°S and asterisk in Figure 5b) exhibit an apparent relief of ~2 km relative to the southern trough floor; the subsidiary trough in northern Candor Chasma is lower by perhaps 1–1.5 km than the floor near Candor Chasma's southern wall. This set of troughs displays a multistage deformational sequence, with western Candor Chasma forming first, followed by faulting and graben formation in Ius Chasma and in northern Candor Chasma (the "subsidiary trough" noted above) [e.g., *Peulvast and Masson*, 1993; *Lucchitta et al.*, 1994; *Schultz*, 1998a].

The best fit to the topography along profile B using the 2-D solution is shown in Figure 6b. In general, the calculated topography matches the slopes and amplitudes of the observed topography reasonably well, and the fault parameters obtained here are not significantly different from those used in the 3-D model (Table 2). Faults in the model for this part of the trough system dip rather shallowly, between 40° and 55°, to depths T_f of 60–75 km. The elevations of plateaus adjacent to Ius Chasma are overpredicted in the model by ~1 km, whereas the plateau north of Candor Chasma is lower than observed by ~500 m. Variations in fault parameters beyond the range given here and in Table 2 lead to substantially poorer fits to the topography, including significant flank uplifts, upwardly bowed trough floors, and steeper plateau slopes. However,

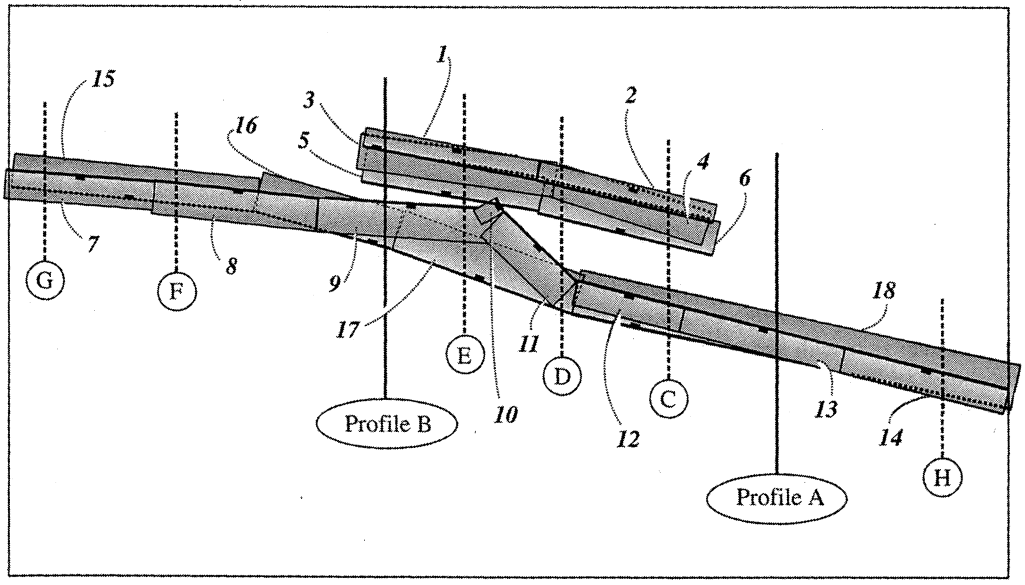

Figure 7. Map showing fault geometries used in 3-D boundary element modeling of the entire trough system. Dashed curves show profiles A–H for which individual boundary element solutions were compared against MOLA topography; numbers denote fault segments in the model (see Table 2). Surface breaks of fault segments are indicated by solid symbols on heavy (solid or dotted) curves. Box shows boundary of calculation grid, spanning ~22° (2°N to 20°S) by ~36° (52°W to 88°W).

the amplitude of trough topography (plateau to floor) discussed here is matched within 4–11% for Ius and Candor Chasmata, suggesting that the fault parameters provide a reasonable first-order estimate of the actual fault configuration.

The best fitting fault parameters for the main Valles Marineris faults are listed in Table 2 and keyed to the map view representation shown in Figure 7. In general, faults bounding the troughs are predicted to dip $\delta = 40°–55°$ to depths of $T_f = 60–75$ km. Fault parameter solutions for all profiles shown in Figure 7 were checked against the available MOLA data, and the results were comparable to those discussed above for profiles A and B. Given reasonable matches between the calculated and observed topographies along the 2-D transects (Figure 7), the three-dimensional deformation field of the planetary surface surrounding the troughs can be calculated by including the combined effects of all faults in the best fitting cross-sectional models.

4.2. Predicted Topography

The origin, spatial distribution, and time dependence of vertical displacements (uplift and subsidence) at the surface caused by offset along normal faults are well known [e.g., *Savage and Hastie*, 1966; *Cohen*, 1999; *King et al.*, 1988; *Willemse*, 1997]. Coseismic (incremental) offset along a normal fault induces subsidence of the surface above the fault plane (forming a basin in the hanging wall) and a smaller amount of uplift of the footwall [*Weissel and Karner*, 1989; *Ma and Kuznir*, 1993; *Willemse*, 1997; *Crider and Pollard*, 1998] (see Figures 3b and 4a). In addition, however, postseismic deformation of the surface due to dip-slip faulting typically occurs over longer timescales when the faulted brittle/elastic layer overlies a viscoelastic channel in the ductile lower crust [*Rundle*, 1982; *King et al.*, 1988; *Freed and Lin*, 1998]. *Freed and Lin* [1998] demonstrated that postseismic stress relaxation in subjacent viscoelastic crust can modify surface elevations behind the fault plane. Although the additional topography associated with such stress relaxation may be difficult to distinguish from postseismic afterslip on the fault without precise geodetic leveling data covering a sufficiently long time period, both sources of postseismic elevation change may contribute to the final (cumulative) surface topography [*Freed and Lin*, 1998]. We use the Coulomb model to calculate the cumulative "coseismic" displacements of the surface (both at the fault and away from it) to model the total surface displacements, strains, and cumulative Coulomb stress changes associated with the total geologic offsets along the faults.

The predicted vertical displacements of the planetary surface surrounding the Valles Marineris were calculated at grid points having a (small) regular spacing of 10 km over an area spanning 1300 by 2150 km (see box, Figure 7), using parameters listed in Tables 1 and 2 and the map view fault geometry shown in Figure 7. The results are shown in Figure 8a as contoured values. The uplift due to cumulative dip-slip offset D along the main trough faults is predicted to be greatest at the trough margins (of order 1 km) and decreases smoothly away toward zero in the cross-strike directions. The predicted uplift is negligible beyond ~250 km from the trough. Ophir Planum and Candor Mensa (asterisk on Figures 1 and 6), located between the Ius-Melas-Coprates and Candor-Ophir Chasma composite troughs, are associated with maximum uplifts of perhaps 1.8 km, with most other regions uplifted only a few hundred meters.

The effect of cumulative dip-slip offset D along trough faults in Valles Marineris is predicted to produce an area of gently elevated topography that parallels the trough system over a distance of ~250 km to either side. Because the predicted induced uplift is generally <500 m beyond the immediate trough vicinity, faulting in the troughs does not appear to have contributed significantly to the regional topography that has been noted as anomalously high [e.g., *Witbeck et al.*, 1991; *Anderson and Grimm*, 1998].

4.3. Horizontal Displacements Across Valles Marineris

Horizontal displacements predicted as a result of localized cumulative fault offsets D were calculated using the same, small, 10-km grid points as the vertical displacements. In the limit of infinitesimally small grid spacing, the predicted displacement field would resemble a continuous array of material points each moving along a vector determined by the aggregate effect of the fault offsets. Adjacent to a fault, the horizontal displacement is maximum and given by $D\cos\delta$ (see Figure 3b). Very far from the fault, the horizontal displacement is negligibly small (St. Venant's principle; *Timoshenko and Goodier* [1970], pp. 39–40) because it is driven by the equivalent of a concentrated load at infinity. At intermediate distances the magnitude of the predicted horizontal displacement depends on the elastic properties of the half-space and on the relative distance to the fault [e.g., *Freund and Barnett*, 1976; *Savage and Hastie*, 1966; *Barnett et al.*, 1987; *Buck*, 1988; *Stein et al.*, 1988; *Weissel and Karner*, 1989; *Okada*, 1992; *Ma and Kusznir*, 1993].

The predicted horizontal component of deformation of the planetary surface, perpendicular to the troughs, is calculated and shown in Figure 8b. Like the distribution of vertical displacement (uplift and subsidence) associated with trough faulting, the predicted horizontal displacement is spatially variable: It is greatest near the troughs, with magnitudes within each 10-km cell exceeding 4–5 km, and decays with distance to < 1 km beyond 250–500 km away.

For normal faults having a $D = 10$ km cumulative offset and dipping at $\delta = 55°$ the (maximum) horizontal displacement across the fault (calculated at the surface using simple trigonometry; see Figure 3b) would be 5 km, suggesting values of 10 km along a traverse across a single graben trough like Coprates Chasma, or 20 km across a two-graben system (e.g., western Coprates Chasma and Candor Chasma) in central Valles Marineris. These values are comparable to those calculated from the 3-D boundary element model for the surface in the vicinity of a trough-bounding normal fault (4–5 km; Figure 8b). However, the predicted horizontal displacements are nonzero away from the troughs, demonstrating that the region surrounding the troughs is influenced by the trough fault offsets D (250–500 km; Figure 8b). This means that the total, cumulative horizontal displacement of rocks at the Martian surface in the Valles Marineris region can exceed the value calculated from trigonometry for the individual fault(s) alone.

Previous work suggested maximum values of horizontal displacement (called "extension" in the previous studies) across the troughs comparable to those reported here. Using Viking topography and fault dip angles of $\delta = 50°–70°$, *Schultz* [1995a] obtained values of ~12–48 km for the center of the trough system and ~5–15 km for its ends. Using dip angles between 40° and 80°, along with estimates of the thicknesses of deposits that partially fill certain troughs, *Mège and Masson* [1996a] independently obtained values ranging from ~45–90 km at trough center to ~5–45 km near the ends. Although uncertainties in topography across the troughs were estimated to be ±1 km in both studies, the major source of uncertainty in these pre-MOLA studies is the fault dip angle δ, leading to considerable variability in the estimates of extension accommodated by the troughs. By comparing the Viking-based topography with available gravity data, *Anderson and Grimm* [1998] inferred values of extension across Valles Marineris of ~70–140 km.

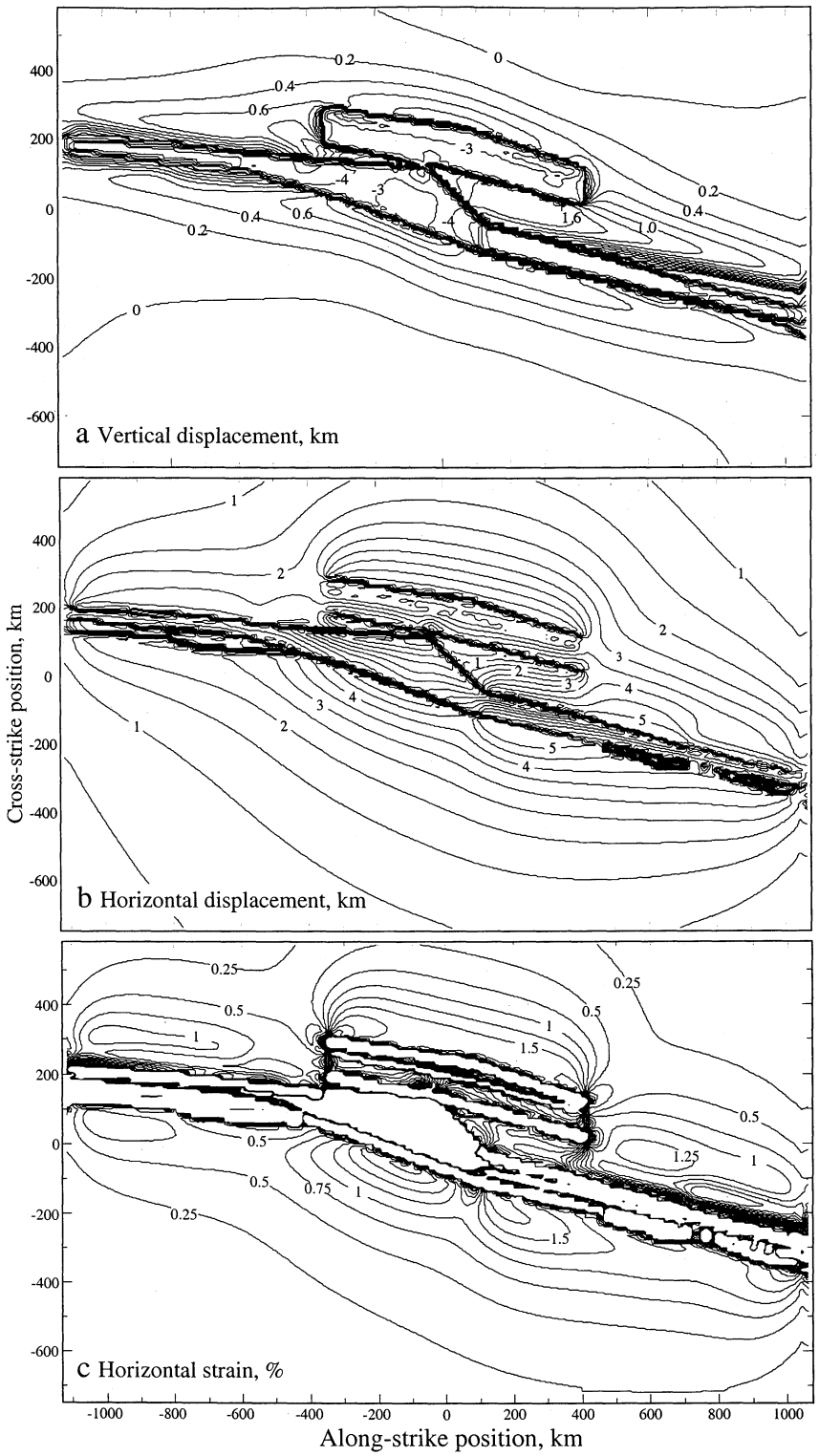

Figure 8. (a) Calculated vertical displacements (uplift and subsidence) associated with cumulative offsets (D) along main Valles Marineris normal faults. (b) Horizontal displacement calculated for the planetary surface for Valles Marineris region. (c) Contour plot showing horizontal strains ε^* predicted for Valles Marineris. Note how predicted strain magnitudes vary with position relative to troughs.

4.4. Extensional Strain

Previous work demonstrates that the strain ε accommodated across faults varies in magnitude with position relative to the fault [e.g., *Freund and Barnett*, 1976; *Cohen*, 1999]. As in the case of horizontal extension, the strain is typically also nonzero in the rock mass surrounding a slipped fault. We estimate values of strain at the planetary surface from the model by explicitly comparing the sizes of grid cells in their initial (undeformed) and final (deformed) states. For cells that are sufficiently small that variations in extension magnitude are negligible within them (i.e., the deformation is homogeneous within the cell), the change in length

of the cell in the direction normal to the troughs gives the predicted strain at that location ($\varepsilon_{cell} = \Delta l/l_i$, where Δl is the change in length and l_i is initial cell length). As in the calculation of displacements, we chose a cell size of 10x10 km^2. This size is small enough that variations in strain magnitude within the cell are negligible, except perhaps in areas of large strain gradients that are predicted to occur at the trough edges (i.e., bounding faults). We note that the magnitudes of strain can vary between cells, leading to an inhomogeneous strain field predicted to be surrounding the fault-bounded troughs. The overall strain field surrounding the Valles Marineris in the model is thus constructed as a piecewise continuous patchwork of locally strained cells.

The predicted horizontal strain field calculated for Valles Marineris is shown in Figure 8c. In general, strains are predicted to be greatest at the trough margins and in the central portion of the trough system; values decrease toward trough ends and with distance perpendicular to the troughs. Because values of vertical strain in each cell (calculated but not shown) are approximately an order of magnitude smaller than the horizontal strains (beyond the troughs), the predicted strain field is dominated by the horizontal component. Predicted horizontal strains are extensional surrounding the troughs, decreasing from maximum values > 10% at the trough walls (corresponding to the bounding normal faults) to < 0.2% beyond ~250 km away from the troughs. Strains are predicted to be negligible beyond ~250 km, or ~2–3 downdip fault heights (or ~4 times the depth of faulting T_f; Table 2), from the troughs. The magnitude of strain from the model is spatially variable and thus inhomogeneous, varying both along-strike and cross-strike relative to the Valles Marineris. The distribution of strain is closely related to that of the predicted horizontal displacement field, given that horizontal strain is the gradient of horizontal displacement.

4.5. Coulomb Stress Change and Secondary Faulting at the Surface

Offset (whether incremental or cumulative) along a fault changes the state of stress in its vicinity, and the magntiude and sense of these inhomogeneous stress perturbations vary with the relative position to the fault [e.g., *Segall and Pollard*, 1980]. Changes in stress state and displacement are greatest near the fault and decrease to negligibly small values at distances of 2–3 fault dimensions (corresponding to the downdip fault heights H in this study) away [e.g., *Segall and Pollard*, 1980; *Barnett et al.*, 1987; *Ma and Kuznir*, 1993]. Cumulative fault offset D leads to changes in the magnitudes of normal and shear stress (σ_n and τ, respectively) resolved on surfaces of given orientation. The Coulomb failure stress, CFS = $|\tau| + \mu\sigma_n$ (where μ is the coefficient of maximum static friction) [e.g., *King et al.*, 1994; *Bruhn and Schultz*, 1996; *Harris*, 1998] explicitly compares the perturbed stress components to the Coulomb frictional sliding criterion to determine if offset on a source fault can trigger or impede frictional sliding on the other faults.

Previous work has demonstrated that lobes of increased Coulomb failure stress develop in directions normal to the fault plane (the "antithetic lobes" of *Freed and Lin* [1998]) as well as parallel to the fault. These lobes of increased Coulomb failure stress are associated in nature with aftershock locations following large earthquakes [e.g., *King et al.*, 1994], suggesting that these lobe-like areas of coseismic stress change can influence regional deformation surrounding the fault. Increased Coulomb failure stress promotes frictional sliding along favorably oriented faults, whereas decreased values can impede offset along these faults [e.g., *King et al.*, 1994; *Harris*, 1998].

Freed and Lin [1998] have evaluated postseismic stress changes associated with fault-induced ductile flow and stress relaxation in subjacent viscous lower crust or upper mantle. They found that Coulomb stress changes near the free surface can increase in magnitude, in some locations, as this time-dependent stress relaxation proceeds, also leading to an increased tendency for offset along optimally oriented surfaces. In addition, they demonstrate that the rate and degree of relaxation in the ductilely flowing layer is greatest immediately beneath the fault and decreases with distance from it. This spatially variable ductile behavior arises from the stress dependence of typical creep laws used to model lower crustal flow [e.g., *Kirby and Kronenberg*, 1987; *Kohlstedt et al.*, 1995] and the stress gradients associated with crustal faulting. Although not incorporated in our boundary element modeling, such inhomogeneous behavior is important when constructing and interpreting lithos-

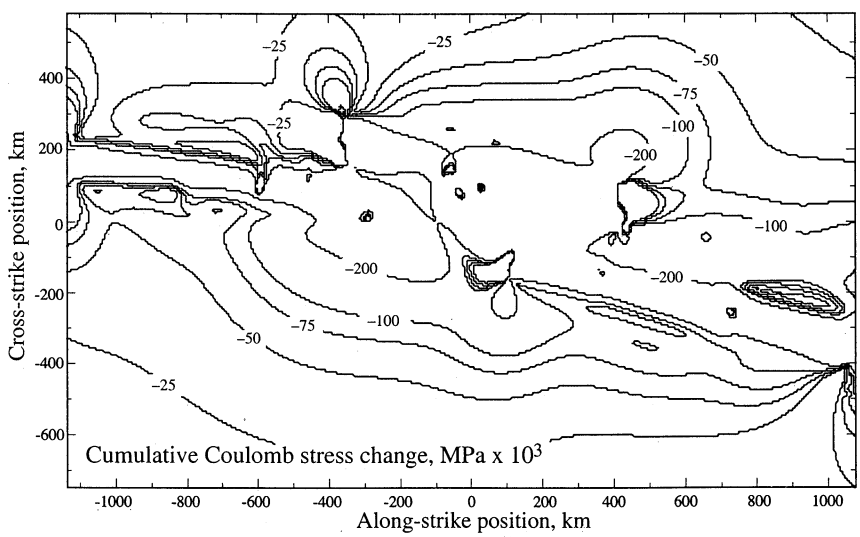

Figure 9. Predicted cumulative Coulomb stress changes for the planetary surface due to cumulative offsets (D) along trough-bounding normal faults, showing areas where nucleation of shallow grabens would be favored (increased cumulative Coulomb failure stresses, positive values) or impeded (decreased cumulative failure stresses, negative values). Contours of cumulative stress change are in MPa x 10^3.

pheric strength envelopes in the vicinity of major faults (see section 5.1).

Predicted changes in cumulative Coulomb failure stress at the surface in the Valles Marineris region are calculated here using the Coulomb modeling code to examine the effect of cumulative offset D along the major trough-bounding normal faults on secondary fractures within near-surface rocks. The predicted cumulative stress changes are calculated for each point on the planetary surface in a horizontal grid having a spacing of 10 km in both the x and y directions. The calculations illustrate cumulative Coulomb stress changes induced by offset along the faults in the absence of confining pressure or tectonic stresses, given that the total stress states associated with normal faulting on Mars are unknown. The addition of confining pressure and/or tectonic stresses may change the orientation of optimal secondary faults and the resulting Coulomb stresses. While the details of the predicted cumulative Coulomb stresses depend on the regional tectonic stresses, the overall stress patterns should remain unchanged. Different values of friction coefficient for the near-surface rock mass (e.g., $0.2 < \mu < 0.8$, Table 1) would not alter the overall stress patterns appreciably.

The results are shown in Figure 9 for the planetary surface. Contours of negative values show areas in which offset is impeded in the model for fractures oriented favorably for normal fault offset (calculated by using a typical friction coefficient $\mu = 0.4$) [e.g., *King et al.*, 1994; *Sibson*, 1994]. Accumulation of offsets D along the main trough-bounding normal faults changes the cumulative local stress state so that even optimally oriented surfaces located within ~250 km of the troughs would be impeded from accumulating normal fault offsets. If this is the case, small normal faults and grabens that are observed in the trough region, including those located on Ophir Planum and parallel to the main troughs [e.g., *Carr*, 1974; *Blasius et al.*, 1977; *Witbeck et al.*, 1991; *Schultz*, 1991, 2000a; *Schultz and Fori*, 1996], probably grew early in the system's development, then became incorporated into the growing Coulomb stress shadow (with impeded frictional slip) as the main trough-bounding faults developed. This inference is consistent with fracture growth simulations in which small fractures grow progressively into larger ones that shield, and inhibit, any smaller fractures from further growth [e.g., *Segall and Pollard*, 1983; *Cladouhos and Marrett*, 1996]. Calculation of cumulative Coulomb stress changes for greater depths ($z = 3$ km, 5 km, and 10 km; not shown) reveals qualitatively similar results, suggesting that, depending on the rates of increase of confining pressure and tectonic stress with depth, normal fault offset along smaller structures may be impeded by the main trough-bounding faults to depths of several kilometers.

5. Discussion and Implications

The results from 3-D boundary element modeling of Valles Marineris troughs provide new insight into the physical behavior of this intriguing region. Here we discuss the implications for lithospheric structure using plausible strength envelopes, local deformation within the troughs, and inhomogeneous strains about Tharsis.

5.1. Lithospheric Structure Beneath Valles Marineris

The 3-D model results imply that the main normal faults bounding Valles Marineris troughs attain depths T_f of 60–75 km, with relatively shallow dips of $\delta = 40°$–$55°$. A series of plausible strength envelopes for extension were constructed given these results by combining brittle and quasi-plastic strength criteria [e.g., *Kohlstedt et al.*, 1995] applicable to the trough region (Figure 10). We note that the Martian geothermal gradient is unconstrained by any measurements, although several model-dependent values have been suggested in the literature [e.g., *Solomon and Head*, 1990; *Anderson and Grimm*, 1998]. Similarly, the thickness of the Martian crust at Valles Marineris is not known, although it is thought to exceed the average global thickness value of $z \sim 50$ km [*Zuber et al.*, 2000] by some amount [e.g., *Banerdt et al.*, 1992; *Anderson and Banerdt*, 2000].

The brittle strength of the Martian faults can be represented by using the Coulomb criterion written in principal stress form [*Kohlstedt et al.*, 1995]. A representative value of fault dip of $\delta = 50°$, as suggested from the modeling results, is shown on Figure 10. Both hydrostatic pore fluid pressures ("wet" on Figure 10) and dry, anhydrous conditions within the Martian crust ("dry" on Figure 10) are shown given the absence of information on pore fluid pressures at the time of faulting.

The tendency for brittle failure of the crust to occur along localized preexisting surfaces (as observed), rather than as distributed cataclastic deformation, is evaluated by comparing the Coulomb frictional strength of the Martian faults to that of crust that lacks throughgoing fault systems [*Kirby and Kronenberg*, 1987]. Localized frictional sliding would occur for likely values of Byerlee frictional resistance [*Sibson*, 1994] (light shading and left-hand curves in Figure 10) that are less than the frictional strength of unfaulted crustal rock (sometimes inaccurately referred to as "intact" rock in the literature; dark shading and right-hand curves in Figure 10); the depth z at which this occurs is the "brittle-ductile transition" [*Kohlstedt et al.*, 1995]. Unfaulted Martian crust is represented by the brittle (frictional) strength of basaltic rock masses using the rock mass rating technique, following *Bieniawski* [1989] and *Schultz* [1996]. A strong rock mass with basaltic composition [e.g., *Mouginis-Mark et al.*, 1992; *Dreibus and Wänke*, 1985; *Bertka and Fei*, 1997] and typical fracture densities (inferred to be comparable to first-order for both planets; see *Schultz* [1993, 1996] for discussion and *McEwen et al.* [1999] for MOC images of layered Martian sequences in Valles Marineris) can be represented by rock mass ratings (RMR [*Bieniawski*, 1989]) of RMR ~ 75 [*Schultz*, 1995b] for anhydrous conditions and RMR ~ 60 for water-saturated conditions. As evident on Figure 10, the Coulomb (frictional) strength of faults that dip at $\delta = 50°$ is much less than that of the surrounding crust ("RMR" in Figure 10) for any degree of pore fluid pressure, indicating that brittle deformation will remain localized, rather than become distributed, to depths of at least 75 km. Fault dips exceeding $\delta = 65°$ with anhydrous conditions along a fault appear necessary for a brittle-ductile transition to develop within $z \sim 90$ km of the Martian surface.

The quasi-plastic strength depends on rock composition, temperature, and strain rate [e.g., *Kirby and Kronenberg*, 1987; *Kohlstedt et al.*, 1995]. For Martian crustal rocks the strength may be approximated by using the creep relation

$$\sigma_d = \left(\frac{\dot{\varepsilon}}{A}\right)^{\frac{1}{n}} \exp\left(\frac{H}{n R T}\right) \quad (1)$$

in which σ_d is the stress difference ($\sigma_v - \sigma_h$ for extension) in MPa for flow, $\dot{\varepsilon}$ is the homogeneous strain rate, n is the power law exponent, A is a material constant, H is the activation enthalpy, R is the gas constant, and T is absolute temperature. We choose parameters appropriate to moist diabase [*Shelton and Tullis*, 1981; cf. *Mackwell et al.*, 1998] with $A = 2.0 \times 10^{-4}$ MPa^{-n} s^{-1}, $n = 3.4$, and $H = 260$ kJ mol^{-1} [*Kirby and Kronenberg*, 1987]. The Martian geothermal gradient for the (late Hesperian-early Amazonian [*Schultz*, 1998]) time

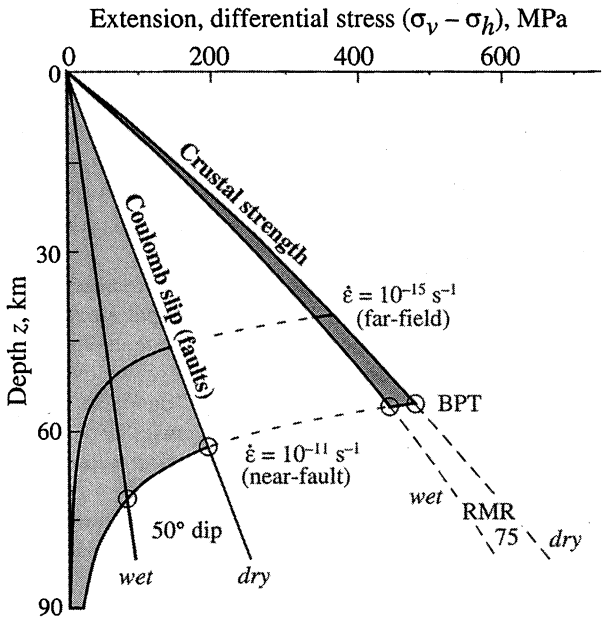

Figure 10. Strength envelope for Valles Marineris trough region consistent with 3-D modeling results. Brittle-plastic transition (BPT) positions are shown as circles on Coulomb slip envelopes for δ = 50° dipping fault (plotted for anhydrous and hydrostatic pore fluid pressures) and on rock mass envelopes for unfaulted Martian crust (anhydrous and hydrostatic). RMR, rock mass ratings. See text for details.

of faulting is taken to be 273 K + 10 K km^{-1} (see discussion below), increasing from approximately near-freezing temperatures at the surface. Strain rates at Valles Marineris are unknown. However, plausible rates can be bounded by two extremes. A slow rate ($\dot{\varepsilon} = 10^{-15}$ s^{-1}) appropriate to gradual planetary cooling or terrestrial continental plate interiors is appropriate to crustal deformation far from faults and other localized sources, whereas faster strain rates ($\dot{\varepsilon} = 10^{-11}$ s^{-1}) [e.g., *Zoback*, 1991] are more appropriate to represent large stress gradients and comparatively rapid deformation in the vicinity of large faults (see *Freed and Lin* [1998] for discussion of spatially variable creep rates). Fast strain rates (and spatially variable strain magnitudes [*Freed and Lin*, 1998; *Albert et al.*, 2000]) are also inferred for lower crust if the faults penetrate through it as "ductile shear zones" [*Kohlstedt et al.*, 1995]. In view of the major ambiguities in strain rate, stability of frictional slip, and spatial variations of stress state near the faults, we choose not to incorporate mantle creep laws to construct a strength envelope for the Valles Marineris lithosphere, notwithstanding the depth of faulting T_f suggested by the 3-D modeling results (T_f < 75 km) being comparable to, or perhaps only somewhat greater than, estimates of the crustal thickness (z > 50 km [*Zuber et al.*, 2000; *Banerdt et al.*, 1992; *Anderson and Banerdt*, 2000]). Mantle flow laws would be necessary to fully characterize the strength and interactions between crust and lithosphere, however, over deeper vertical sections and in areas far from the trough faults where a constant, homogeneous strain rate throughout the entire lithospheric section would be more appropriate [e.g., *Albert et al.*, 2000].

The estimated strength envelope for the Martian crust in the trough region (Figure 10) is generally consistent with the approximate depth of faulting inferred from the 3-D boundary element model (T_f = ~60–75 km) for two conditions: a Martian geothermal gradient less than ~10 K km^{-1} and strain rates of the order of 10^{-11} s^{-1}. Higher geothermal gradients and/or slower homogeneous strain rates would decrease the depth z of the peak strength in the semibrittle region where brittle and quasi-plastic criteria intersect (brittle-plastic transition (BPT, circles in Figure 10) from z ~ 60 km to values perhaps half this deep. However, faster strain rates should be anticipated in actively deforming regions, like the Valles Marineris, rather than slow homogeneous background values characteristic of tectonically dormant regions, as long as the rate of faulting exceeds that of lower crustal relaxation. Given that yield strength envelopes do not consider spatially variable flexural rigidities (or equivalently, effective elastic thicknesses) typical of the near-fault environment [*Buck*, 1988], or depth- (and temperature-) dependent frictional stability of crustal-scale faults [*Tse and Rice*, 1986], the previous results obtained from long-wavelength spatial averages (~600 km) by *Anderson and Grimm* [1998] are likely unrevealing of the detailed lithospheric structure beneath the troughs. Similarly, although large values for geothermal gradient (>> 10 K km^{-1}) have been proposed [e.g., *Solomon and Head*, 1990; *Anderson and Grimm*, 1998], the evidence for extensive volcanism in the troughs is equivocal during the most recent period of large-scale faulting analyzed in this paper [*Lucchitta et al.*, 1992; *Schultz*, 1998a]. Explicit modeling of rift flank uplifts using plausible ranges of geothermal gradients and crustal structures by *Chèry et al.* [1992] and *Brown and Phillips* [1999] suggests that this surface topography may not be sensitive to geothermal gradient alone. Thus comparatively low geothermal gradients suggested by our models appear to be consistent with the geologic observations although larger ones may not be ruled out given the ambiguities in local strain rate at the troughs.

5.2. Erosional Versus Structural Trough Widths

Previous work suggested that the troughs have been widened by erosional retreat of fault surfaces by perhaps a factor of 3. The best fitting fault dips obtained in this paper are considerably shallower (δ = 40° at the southern wall and δ = 55° at the northern wall) than those used previously (δ > 60° [*Lucchitta et al.*, 1994; see also *Schultz*, 1991, 1995a and *Mége and Masson*, 1996c]) to evaluate the degree of erosional widening of the troughs. Using the shallower dip angles, the degree of erosional widening implied by map view morphology (Figure 1) is reduced. For example, the central section of Coprates Chasma along 65°W has structural widths of W_s = 45 km for the graben floor and W_e = 110 km for the eroded trough (measured from *Witbeck et al.* [1991]), leading to W_s/W_e = 0.4 if the trough depth and fault dip are not considered. Using the best fitting fault dips for profile A (δ = 55° for the northern fault and δ = 40° for the southern fault) and restoring to the same elevation using the fault offsets, however, W_s/W_e = 0.6. Thus the structural width of central Coprates Chasma is ~60% of its erosional width, rather than ~30% as used in some previous studies. Shallower faults require less material to be removed by erosion than previously thought [cf. *Lucchitta et al.*, 1994], and the mass deficit due to faulting is associated with a larger fraction of the observed topography.

5.3. Deformation Within the Troughs by Late Stage Faulting

The fault parameters for central Coprates Chasma (Table 2 and Figure 6) are consistent with a graben floor that is relatively undeformed. In contrast, however, the best fitting fault parameters for the more complex, three-graben configuration in profile B imply that the intervening plateaus and basins were deformed by trough faulting. A cross section drawn using the MOLA topography data

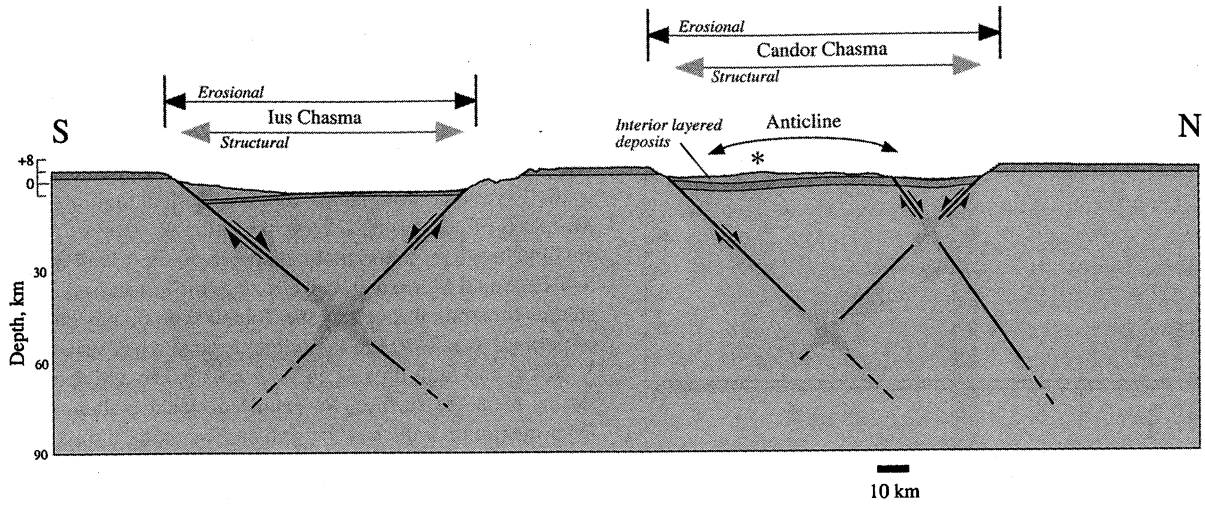

Figure 11. Geologic cross section through central Ius and westernmost Candor Chasmata (profile B) based on best fitting fault parameters and the 3-D model results. Fault intersections are schematic and do not include small-scale structures associated with geologically synchronous displacement accumulation along the main faults. Asterisk indicates position of Candor Mensa.

(orbit 25), best fitting fault parameters, and no vertical exaggeration is shown in Figure 11. In this region the structural widths are a close approximation of the erosional widths: $W_s/W_e = 0.94$ for Ius Chasma and $W_s/W_e = 0.9$ for Candor Chasma. Here the predicted surface topography in Candor Chasma is influenced by the small, north dipping fault along its southern margin. The calculated topography using the best fitting fault parameters suggests that the Candor Chasma basin, and the sequence of interior layered deposits that predate at least some of the trough faulting, might have been deformed into an anticline (Figure 11) as offsets accumulated along the main normal faults. Trough faulting provides a plausible mechanism for deforming and tilting the interior layered deposits within the ancestral basins as has been observed [e.g., *Lucchitta*, 1990, 1999; *Peulvast and Masson*, 1993]. We hypothesize that spatial variations in deformation within the troughs may be related to the geometry and offset distribution of the underlying trough-bounding normal faults.

Forward modeling of the trough topography at Valles Marineris suggests that the main normal faults can reach depths T_f of 60–75 km with uniform dips δ of 40°–55°. Together with observed trough widths, the faults may intersect at shallower depths z (Figure 11). As long as the faults are geologically synchronous [*Nicol et al.*, 1995; *Ferrill et al.*, 2000], however, the cumulative offset distributions [*Maerten et al.*, 1999] and geometry can be maintained. Cumulative offsets D along faults that were significantly less deep (smaller T_f), or nonplanar (e.g., listric), would not predict displacements of the Martian surface that resemble the observed topography. We envision that the fault intersection region at depth is a network of crosscutting fault strands that developed as dip-slip offsets localized repeatedly along the preexisting faults.

5.4. Strain Distribution Surrounding Tharsis

Several studies have attempted to quantify the magnitude and distribution of extensional strain in the Tharsis province [e.g., *Plescia*, 1991; *Schultz*, 1995a; *Mége and Masson*, 1996c; *Golombek et al.*, 1996] in order to provide observational bounds on predicted values of elastic strain ε_0 from geodynamic models [e.g., *Banerdt et al.*, 1992; *Tanaka et al.*, 1991; *Mége and Masson*, 1996a]. Significantly, however, *Plescia* [1991], *Schultz* [1995a], and *Mége and Masson* [1996c] found that the magnitudes of strains reported in some studies varied inversely with traverse length, implying that the traverse lengths used in previous studies (~1000 km or more) exceed those required to accurately represent homogeneous strains [*Jamison*, 1989; *Wojtal*, 1989]. This means that larger strains near grabens were inadvertently averaged with much smaller strains in areas far from faults to produce the reported strains of << 1% across graben systems [*Golombek et al.*, 1996]. As a result, the low strain values suggested for Tharsis radial graben sets [e.g., *Plescia*, 1991; *Golombek et al.*, 1996] critically underestimate the actual magnitude of extensional strain that is recorded in those structures (see also discussions of homogeneous and apparent strains across faulted terranes by *Jamison* [1989], *Wojtal* [1989], and *Schultz* [2000a]).

Values of vertical displacement, horizontal displacement, and horizontal strain calculated along profile A (the cross-strike direction) are compared in Figures 12a and 12b. All three quantities are predicted to vary spatially relative to the troughs. The predicted horizontal displacement is extensional everywhere (except within the troughs; shaded area in Figure 12a) and typically exceeds the magnitude of uplift (positive vertical displacement) by a factor of 5–10. The inhomogeneous strains ε^* predicted by the full 3-D boundary element model for the Valles Marineris region (Figure 8c) are spatially variable, with local maximum values of $\varepsilon^* > 10\%$ at the trough walls that compare favorably with previous Viking-based results that assumed sufficiently small traverse lengths [*Schultz*, 1995a]. Away from the trough faults, however, the magnitude of predicted horizontal strain in the trough region is much smaller, typically $\varepsilon^* < 1$–2% (Figures 12b and 8c). The predicted horizontal strain thus varies spatially, decreasing in magnitude with cross-strike distance from the troughs to $\varepsilon^* < 0.2\%$ beyond ~250 km (Figure 12b).

The cumulative horizontal displacement predicted across the Valles Marineris region is estimated by summing the individual horizontal displacements obtained from each cell in the cross-strike direction. Cumulative horizontal displacement is predicted to vary spatially, from ~50–100 km through the trough's western and eastern terminations, respectively, to ~200 km through the trough's

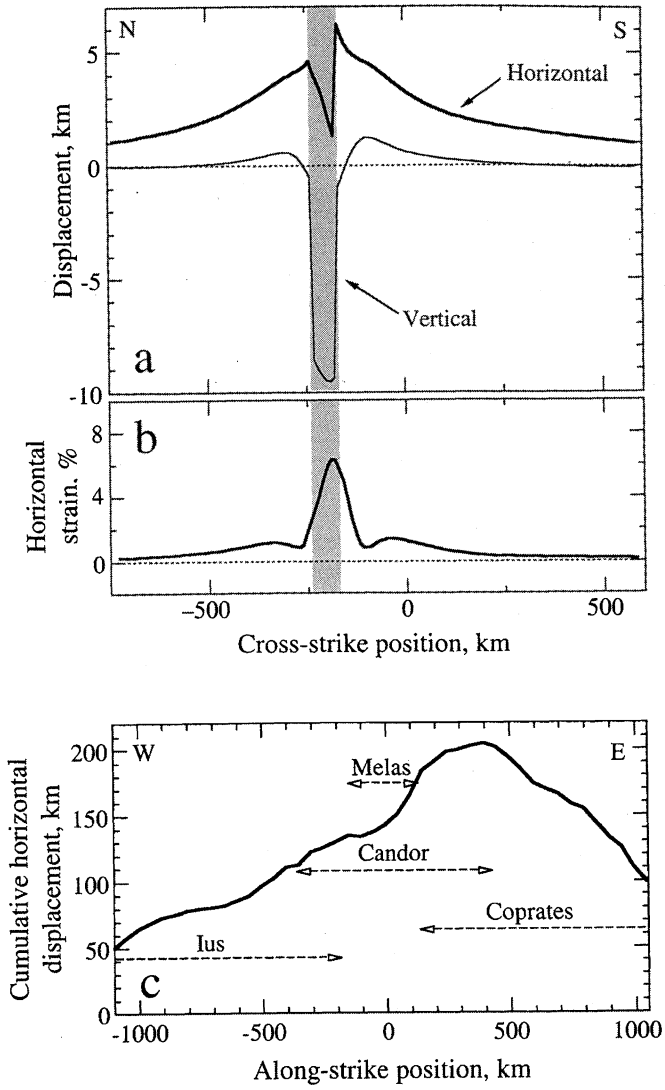

Figure 12. (a) Predicted variation of vertical displacement, horizontal displacement, and horizontal strain ε^* calculated across central Coprates Chasma (profile A). Note that the horizontal component of displacement predicted for the surface ("extension") typically exceeds the vertical component (uplift or subsidence) by about a factor of 5, except within the trough. Strains are greatest at the troughs and decrease significantly in magnitude with perpendicular distance. (b) Cumulative horizontal displacement summed in the cross-strike direction. Note similarity to structural relief of the composite trough shown in Figure 2b. Approximate locations of major troughs are indicated.

central region (Figure 12c). This range is comparable to, or somewhat greater than, the values of total trough "extension" in the literature [*Schultz*, 1995a; *Mège and Masson*, 1996a; *Anderson and Grimm*, 1998]. Dividing the cumulative horizontal displacement by the perpendicular traverse length (~1300 km; Figure 8) leads to average values of province-wide strain of $\varepsilon^* = 4$–15%, which are comparable to those reported by *Schultz* [1995a]. The remarkably good correspondence between the average province strain predicted by the boundary element model (which includes deformation beyond the trough-bounding faults) and the previous values (which neglect off-fault deformation) confirms that a large fraction of the strain in the Valles Marineris region occurs along the largest normal faults [e.g., *Scholz and Cowie*, 1990] (as suggested for Mars by *Schultz* [2000a] on the basis of fault population statistics).

The predicted strain field for the Valles Marineris grabens implies that small Martian grabens, having segment lengths of tens of kilometers, widths of several kilometers, and throws of perhaps 100–500 m [*Davis et al.*, 1995; *Schultz*, 1997], should also exhibit spatially variable strain fields. Given a depth of faulting T_f at Valles Marineris of perhaps 60–75 km, the strain ε^* decays to negligibly small values over a horizontal distance of ~3–4 fault depths (i.e., 3–4 T_f). Small Martian grabens, such as those assessed in previous studies for strain throughout the Tharsis region, may attain depths of perhaps $T_f = 3$–10 km (assuming typical cross-strike widths of 5–10 km and fault dips of $50° < \delta < 65°$). We anticipate that the strains ε^* at the surface, for each individual graben, will decay from maximum values at the graben (assuming a traverse length less than or equal to graben width) to negligibly small values over a horizontal distance of perhaps 15–40 km. The aggregate strain field surrounding Tharsis is likely a highly variable spatial composite of the inhomogeneous strain fields associated with each of the many grabens. The current, inhomogeneous strain field (as inferred, for example, from the fault population statistics [*Schultz*, 2000a]) likely developed by nucleation and lateral spreading of graben-centered fault strain fields as the grabens themselves grew in length and offset magnitude.

6. Conclusions

The 3-D boundary element modeling of Valles Marineris, combined with new measurements of trough topography from MOLA, permit a geodetic inversion of the trough topography for fault geometry in the Martian crust. Although the form of the along-strike distribution of throws for the main Ius-Melas-Coprates Chasma graben is similar in character to previous determinations, the fault dips are found to be significantly shallower than previously recognized, leading to larger values of horizontal (extensional) displacement for given values of trough relief than previously estimated. The small degree of footwall uplift (< 500 m) measured along the troughs, combined with the trough widths and dip-slip fault offsets, suggests faults that penetrate to depths of $T_f = 60$–75 km with dip angles of $\delta = 40°$–55°. These depths in turn imply relatively cool geothermal gradients at the time of faulting, perhaps 10 K km^{-1} or less (depending on the local strain rate at the troughs), consistent with the apparent paucity of volcanism during trough faulting. Calculations of cumulative Coulomb stress changes predicted to accompany trough fault offsets suggest that small grabens on plateaus adjacent to the troughs formed early, before the main troughs attained their current extent, and that extensional deformation in regions surrounding the troughs probably ceased during a late stage of trough growth.

Given the new values of bounding-fault geometry, the structural troughs were widened erosionally by at most a factor of 2 (at Coprates Chasma) to <10% in other troughs. Estimates of volumes of eroded wall rock, based on a Viking era factor of 3 widening, thus require substantial downward revision. Shallow normal faults beneath the Candor-Ophir composite trough in particular may be associated with anticlinal flexure of the preexisting interior layered deposits and attendant fracturing, as recently noted in detailed mapping studies of trough interiors. The predicted regional strain field is greatest at the trough-bounding faults and decays with cross-strike distance; this inhomogeneous strain field likely also typifies the effect of smaller Martian grabens on the overall strain field surrounding Tharsis.

Acknowledgments. This work was supported by grants from the NASA Planetary Geology and Geophysics Program and the Mars Data Analysis Program. Thorough reviews by Juliet Crider, Bruce Banerdt, and the Associate Editor improved the clarity and precision of the final paper. Discussions with Scott Anderson and Roger Phillips on continuum models of Valles Marineris led to refinements in understanding its geodynamics. A pleasant sabbatical visit to the Woods Hole Oceanographic Institution (WHOI) by the first author during parts of the 1998–1999 academic year facilitated the work. Presentation of preliminary results to colleagues at the NASA Goddard Space Flight Center, including Herb Frey, Dave Harding, and Steve Cohen, helped to clarify the importance of several factors in the dislocation modeling of fault-related topography. Scott Wilkins and Daniel Mège helped with the MOLA data. Ross Stein kindly made available the Coulomb boundary element program. This is WHOI contribution 10312.

References

Albert, R.A., R.J. Phillips, A.J. Dombard, and C.D. Brown, A test of the validity of yield strength envelopes with an elastoviscoplastic finite element model, *Geophys. J. Int.*, *140*, 399–409, 2000.

Anderson, F.S., and W.B. Banerdt, Preliminary admittance estimates for the Valles Marineris, Mars, *Lunar Planet. Sci.* [CD-ROM], *XXXI*, abstract 2090, 2000.

Anderson, F.S., and R.E. Grimm, Rift processes at the Valles Marineris, Mars: Constraints from gravity on necking and rate-dependent strength evolution, *J. Geophys. Res.*, *103*, 11,113–11,124, 1998.

Baker, V.R., M.H. Carr, V.C. Gulick, C.R. Williams, and M.S. Marley, Channels and valley networks, in *Mars*, edited by H.H. Kieffer et al., pp. 493–522, Univ. of Ariz. Press, Tucson, 1992.

Banerdt, W.B., M.P. Golombek, and K.L. Tanaka, Stress and tectonics on Mars, in *Mars*, edited by H.H. Kieffer et al., pp. 249–297, Univ. of Ariz. Press, Tucson, 1992.

Barnett, J.A.M., J. Mortimer, J.H. Rippon, J.J. Walsh, and J. Watterson, Displacement geometry in the volume containing a single normal fault, *AAPG Bull.*, *71*, 925–937, 1987.

Bertka, C.M., and Y. Fei, Mineralogy of the Martian interior up to core-mantle boundary pressures, *J. Geophys. Res.*, *102*, 5251–5264, 1997.

Bieniawski, Z.T., *Engineering Rock Mass Classifications*, 251 pp., John Wiley, New York, 1989.

Blasius, K.R., J.A. Cutts, J.E. Guest, and H. Masursky, Geology of the Valles Marineris: First analysis of imaging from the Viking 1 Orbiter primary mission, *J. Geophys. Res.*, *82*, 4067–4091, 1977.

Brown, C.D., and R.J. Phillips, Flexural rift flank uplift at the Rio Grande rift, New Mexico, *Tectonics*, *18*, 1275–1291, 1999.

Bruhn, R.L., and R.A. Schultz, Geometry and slip distribution in normal fault systems: Implications for mechanics and fault-related hazards, *J. Geophys. Res.*, *101*, 3401–3412, 1996.

Buck, W.R., Flexural rotation of normal faults, *Tectonics*, *7*, 959–973, 1988.

Carr, M.H., Tectonism and volcanism of the Tharsis region of Mars, *J. Geophys. Res.*, *79*, 3943–3949, 1974.

Carr, M.H., Retention of an atmosphere on early Mars, *J. Geophys. Res.*, *104*, 21,897–21,909, 1999.

Chéry, J., F. Lucazeau, M. Daignières, and J.P. Vilotte, Large uplift of rift flanks: A genetic link with lithosphere rigidity?, *Earth Planet. Sci. Lett.*, *112*, 195–211, 1992.

Cladouhos, T.T., and R. Marrett, Are fault growth and linkage models consistent with power-law distributions of fault lengths?, *J. Struct. Geol.*, *18*, 281–293, 1996.

Clifford, S.M., A model for the hydrologic and climatic behavior of water on Mars, *J. Geophys. Res.*, *98*, 10,973–11,016, 1993.

Cohen, S.C., Numerical models of crustal deformation in seismic zones, *Adv. Geophys.*, *41*, 133–231, 1999.

Crider, J.G., and D.D. Pollard, Fault linkage: Three-dimensional mechanical interaction between echelon normal faults, *J. Geophys. Res.*, *103*, 24,373–24,391, 1998.

Dade, W.B., and H.E. Huppert, Long-runout rockfalls, *Geology*, *26*, 803–806, 1998.

Davis, P.A., K.L. Tanaka, and M.P. Golombek, Topography of closed depressions, scarps, and grabens in the north Tharsis region of Mars: Implications for shallow crustal discontinuities and graben formation, *Icarus*, *114*, 403–422, 1995.

Dohm, J.M., and K.L. Tanaka, Geology of the Thaumasia region, Mars: Plateau development, valley origins, and magmatic evolution, *Planet. Space Sci.*, *47*, 411–431, 1999.

Dohm, J.M., R.C. Anderson, and K.L. Tanaka, Digital structural mapping of Mars, *Astron. Geophys.*, *39*, 3.20–3.22, 1998.

Dreibus, G., and H. Wänke, Mars: A volatile-rich planet, *Meteoritics*, *20*, 367–382, 1985.

Ferrill, D.A., A.P. Morris, J.A. Stamatakos, and D.W. Sims, Crossing conjugate normal faults, *AAPG Bull.*, *84*, 1543–1559, 2000.

Freed, A.M., and J. Lin, Time-dependent changes in failure stress following thrust earthquakes, *J. Geophys. Res.*, *103*, 24,393–24,409, 1998.

Freund, L.B., and D.M. Barnett, A two-dimensional analysis of surface deformation due to dip-slip faulting, *Bull. Seismol. Soc. Am.*, *66*, 667–675, 1976.

Frey, H., Thaumasia: A fossilized early forming Tharsis uplift, *J. Geophys. Res.*, *84*, 1009–1023, 1979.

Golombek, M.P., K.L. Tanaka, and B.J. Franklin, Extension across Tempe Terra, Mars, from measurements of fault scarp widths and deformed craters, *J. Geophys. Res.*, *101*, 26,119–26,130, 1996.

Harris, R.A., Introduction to special section: Stress triggers, stress shadows, and implications for seismic hazard, *J. Geophys. Res.*, *103*, 24,347–24,358, 1998.

Jamison, W.R., Fault-fracture strain in Wingate Sandstone, *J. Struct. Geol.*, *11*, 959–974, 1989.

King, G.C.P., R.S. Stein, and J.B. Rundle, The growth of geological structures by repeated earthquakes, 1, Conceptual framework, *J. Geophys. Res.*, *93*, 13,307–13,318, 1988.

King, G.C.P., R.S. Stein, and J. Lin, Static stress changes and the triggering of earthquakes, *Bull. Seismol. Soc. Am.*, *84*, 935–953, 1994.

Kirby, S.H., and A.K. Kronenberg, Rheology of the lithosphere: Selected topics, *Rev. Geophys.*, *25*, 1219–1244, 1987. (Correction, *Rev. Geophys.*, *25*, 1680–1681, 1987.)

Kohlstedt, D.L., B. Evans, and S.J. Mackwell, Strength of the lithosphere: Constraints imposed by laboratory experiments, *J. Geophys. Res.*, *100*, 17,587–17,602, 1995.

Komatsu, G., P.E. Geissler, R.G. Strom, and R.B. Singer, Stratigraphy and erosional landforms of layered deposits in Valles Marineris, Mars, *J. Geophys. Res.*, *98*, 11,105–11,121, 1993.

Ladbury, R., Rediscovering Mars, *Phys. Today*, *52*, 33–35, 1999.

Lucchitta, B.K., Landslides in Valles Marineris, Mars, *J. Geophys. Res.*, *84*, 8079–8113, 1979.

Lucchitta, B.K., Young volcanic deposits in the Valles Marineris, Mars?, *Icarus*, *86*, 476–509, 1990.

Lucchitta, B.K., Geologic map of Ophir and central Candor Chasmata (MTM –05072) of Mars, scale 1:500,000, *U.S. Geol. Surv. Misc. Invest. Map*, *I–2568*, 1999.

Lucchitta, B.K., A.S. McEwen, G.D. Clow, P.E. Geissler, R.B. Singer, R.A. Schultz, and S.W. Squyres, The canyon system on Mars, in *Mars*, edited by H.H. Kieffer et al., pp. 453–492, Univ. of Ariz. Press, Tucson, 1992.

Lucchitta, B.K., N.K. Isbell, and A. Howington-Kraus, Topography of Valles Marineris: Implications for erosional and structural history, *J. Geophys. Res.*, *99*, 3783–3798, 1994.

Ma, X.Q., and N.J. Kusznir, Modelling of near-field subsurface displacements for generalized faults and fault arrays, *J. Struct. Geol.*, *15*, 1471–1484, 1993.

Mackwell, S.J., M.E. Zimmerman, and D.L. Kohlstedt, High-temperature deformation of dry diabase with application to tectonics on Venus, *J. Geophys. Res.*, *103*, 975–984, 1998.

Maerten, L., E.J.M. Willemse, D.D. Pollard, and K. Rawnsley, Slip distributions on intersecting normal faults, *J. Struct. Geol.*, *21*, 259–271, 1999.

McEwen, A.S., Mobility of large rock avalanches: Evidence from Valles Marineris, Mars, *Geology*, *17*, 1111–1114, 1989.

McEwen, A.S., M.C. Malin, M.H. Carr, and W.K. Hartmann, Voluminous volcanism on early Mars revealed in Valles Marineris, *Nature*, *397*, 584–586, 1999.

Mège, D., Aspects structuraux du complexe magmato-tectonique de Tharsis sur Mars, thèse de doctorat (in French), 382 pp., Lab. de Géol. Dyn. de la Terre et des Planètes, Univ. de Paris-Sud, Orsay, France, 1994.

Mège, D., and P. Masson, Stress models for Tharsis formation, Mars, *Planet. Space Sci.*, *44*, 1471–1497, 1996a.

Mège, D., and P. Masson, A plume tectonics model for the Tharsis province, Mars, *Planet. Space Sci.*, *44*, 1499–1546, 1996b.

Mège, D., and P. Masson, Amounts of crustal stretching in Valles Marineris, Mars, *Planet. Space Sci.*, *44*, 749–782, 1996c.

Mouginis-Mark, P.J., L. Wilson, and M.T. Zuber, The physical volcanology of Mars, in *Mars*, edited by H.H. Kieffer et al., pp. 424–452, Univ. of Ariz. Press, Tucson, 1992.

Nedell, S.S., S.W. Squyres, and D.W. Andersen, Origin and evolution of

the layered deposits in the Valles Marineris, Mars, *Icarus*, *70*, 409–441, 1987.

Nicol, A., J.J. Walsh, J. Watterson, and P.G. Bretan, Three-dimensional geometry and growth of conjugate normal faults, *J. Struct. Geol.*, *17*, 847–862, 1995.

Okada, Y., Internal deformation due to shear and tensile faults in a half-space, *Bull. Seismol. Soc. Am.*, *82*, 1018–1040, 1992.

Peulvast, J.P., and P.L. Masson, Erosion and tectonics in central Valles Marineris (Mars): A new morpho-structural model, *Earth Moon Planets*, *61*, 191–217, 1993.

Plescia, J.B., Graben and extension in northern Tharsis, Mars, *J. Geophys. Res.*, *96*, 18,883–18,895, 1991.

Plescia, J.B., and R.S. Saunders, Tectonic history of the Tharsis region, Mars, *J. Geophys. Res.*, *87*, 9775–9791, 1982.

Rudnicki, J.W., Fracture mechanics applied to the Earth's crust, *Annu. Rev. Earth Planet. Sci.*, *8*, 489–525, 1980.

Rundle, J.B., Viscoelastic-gravitational deformation by a rectangular thrust fault in a layered earth, *J. Geophys. Res.*, *87*, 7787–7796, 1982.

Savage, J.C., and L.M. Hastie, Surface deformation associated with dip-slip faulting, *J. Geophys. Res.*, *71*, 4897–4904, 1966.

Scholz, C.H., and P.A. Cowie, Determination of geologic strain from fault slip data, *Nature*, *346*, 837–839, 1990.

Schultz, R.A., Structural development of Coprates Chasma and western Ophir Planum, central Valles Marineris rift, Mars, *J. Geophys. Res.*, *96*, 22,777–22,792, 1991.

Schultz, R.A., Brittle strength of basaltic rock masses with applications to Venus, *J. Geophys. Res.*, *98*, 10,883–10,895, 1993.

Schultz, R.A., Gradients in extension and strain at Valles Marineris, Mars, *Planet. Space Sci.*, *43*, 1561–1566, 1995a.

Schultz, R.A., Limits on strength and deformation properties of jointed basaltic rock masses, *Rock Mech. Rock Eng.*, *28*, 1–15, 1995b.

Schultz, R.A., Relative scale and the strength and deformability of rock masses, *J. Struct. Geol.*, *18*, 1139–1149, 1996.

Schultz, R.A., Displacement-length scaling for terrestrial and Martian faults: Implications for Valles Marineris and shallow planetary grabens, *J. Geophys. Res.*, *102*, 12,009–12,015, 1997.

Schultz, R.A., Multiple-process origin of Valles Marineris basins and troughs, Mars, *Planet. Space Sci.*, *46*, 827–834, 1998a.

Schultz, R.A., Geologic map of MTM –10067 quadrangle of the western Coprates Chasma region of Mars, scale 1:500,000, *U.S. Geol. Surv. Misc. Invest. Map*, *I–2588*, 1998b.

Schultz, R.A., Fault-population statistics at the Valles Marineris Extensional Province, Mars: Implications for segment linkage, crustal strains, and its geodynamic development, *Tectonophysics*, *316*, 169–193, 2000a.

Schultz, R.A., Localization of bedding plane slip and backthrust faults above blind thrust faults: Keys to wrinkle ridge structure, *J. Geophys. Res.*, *105*, 12,035–12,052, 2000b.

Schultz, R.A., and A.N. Fori, Fault-length statistics and implications of graben sets at Candor Mensa, Mars, *J. Struct. Geol.*, *18*, 373–383, 1996.

Segall, P., and D.D. Pollard, Mechanics of discontinuous faults, *J. Geophys. Res.*, *85*, 4337–4350, 1980.

Segall, P., and D.D. Pollard, Joint formation in granitic rock of the Sierra Nevada, *Geol. Soc. Am. Bull.*, *94*, 563–575, 1983.

Shelton, G., and J. Tullis, Experimental flow laws for crustal rocks (abstract), *Eos Trans. AGU*, *62*, 396, 1981.

Sibson, R.H., An assessment of field evidence for 'Byerlee' friction, *Pure Appl. Geophys.*, *142*, 645–662, 1994.

Smith, D.E., et al., Topography of the northern hemisphere of Mars from the Mars Orbiter Laser Altimeter, *Nature*, *279*, 1686–1692, 1998.

Smith, D.E., et al., The global topography of Mars and implications for surface evolution, *Science*, *284*, 1495–1503, 1999.

Solomon, S.C., and J.W. Head, Heterogeneities in the thickness of the elastic lithosphere of Mars: Constraints on heat flow and internal dynamics, *J. Geophys. Res.*, *95*, 11,073–11,083, 1990.

Spencer, J.R., and F.P. Fanale, New models for the origin of Valles Marineris closed depressions, *J. Geophys. Res.*, *95*, 14,301–14,313, 1990.

Stein, R.S., G.C. King, and J.B. Rundle, The growth of geological structures by repeated earthquakes 2, Field examples of continental dip-slip faults, *J. Geophys. Res.*, *93*, 13,319–13,331, 1988.

Taboada, A., J.C. Bousquet, and H. Philip, Coseismic elastic models of folds above blind thrusts in the Betic Cordilleras (Spain) and evaluation of seismic hazard, *Tectonophysics*, *220*, 223–241, 1993.

Tanaka, K.L., and P.A. Davis, Tectonic history of the Syria Planum province of Mars, *J. Geophys. Res.*, *93*, 14,893–14,917, 1988.

Tanaka, K.L., M.P. Golombek, and W.B. Banerdt, Reconciliation of stress and structural histories of the Tharsis region of Mars, *J. Geophys. Res.*, *96*, 15,617–15,633, 1991.

Timoshenko, S.P., and J.N. Goodier, *Theory of Elasticity*, 567 pp., McGraw-Hill, New York, 1970.

Toda, S., R.S. Stein, P.A. Reasenberg, J.H. Dieterich, and A. Yoshida, Stress transferred by the 1995 M_w = 6.9 Kobe, Japan, shock: Effect on aftershocks and future earthquake probabilities, *J. Geophys. Res.*, *103*, 24,543–24,565, 1998.

Tse, S.T., and J.R. Rice, Crustal earthquake instability in relation to the depth variation of frictional slip processes, *J. Geophys. Res.*, *91*, 9452–9472, 1986.

Watters, T.R., Compressional tectonism on Mars, *J. Geophys. Res.*, *98*, 17,049–17,060, 1993.

Weissel, J.K., and G.D. Karner, Flexural uplift of rift flanks due to mechanical unloading of the lithosphere during extension, *J. Geophys. Res.*, *94*, 13,919–13,950, 1989.

Willemse, E.J.M., Segmented normal faults: Correspondence between three-dimensional mechanical models and field data, *J. Geophys. Res.*, *102*, 675–692, 1997.

Witbeck, N.E., K.L. Tanaka, and D.H. Scott, Geologic map of the Valles Marineris region, Mars, scale 1:2,000,000, *U.S. Geol. Surv. Misc. Invest. Map*, *I–2010*, 1991.

Wojtal, S.F., Measuring displacement gradients and strains in faulted rocks, *J. Struct. Geol.*, *11*, 669–678, 1989.

Zoback, M.D., State of stress and crustal deformation along weak transform faults, *Philos. Trans. R. Soc. London, ser. A*, *337*, 141–150, 1991.

Zuber, M.T., D.E. Smith, S.C. Solomon, D.O. Muhleman, J.W. Head, J.B. Garvin, J.B. Abshire, and J.L. Bufton, The Mars Observer Laser Altimeter investigation, *J. Geophys. Res.*, *97*, 7781–7797, 1992.

Zuber, M.T., et al., Internal structure and early thermal evolution of Mars from Mars Global Surveyor topography and gravity, *Science*, *287*, 1788–1793, 2000.

J. Lin, Department of Geology and Geophysics, MS 22, Woods Hole Oceanographic Institution, Woods Hole, MA 02543. (jlin@whoi.edu)

R.A. Schultz, Geomechanics–Rock Fracture Group, Department of Geological Sciences/172, Mackay School of Mines, University of Nevada, Reno NV 89557–0138. (schultz@mines.unr.edu)

(Received July 11, 2000; revised February 7, 2001;
accepted February 14, 2001.)